

## Development of the online MM5 tracer model and its applications to air pollution episodes in Istanbul, Turkey and Sahara dust transport

S.-H. Chen,<sup>1,2</sup> J. Dudhia,<sup>3</sup> J. S. Kain,<sup>4</sup> T. Kindap,<sup>5</sup> and E. Tan<sup>6,7</sup>

Received 24 July 2007; revised 21 November 2007; accepted 13 February 2008; published 6 June 2008.

[1] An online tracer model, based on the fifth-generation Penn State/NCAR Mesoscale model, was developed. The new model includes full representation of processes for advection, boundary layer mixing, subgrid cumulus convective mixing, and sedimentation of tracers. The model was used in two very different applications to document its potential utility. The first application involves pollutant transport to Istanbul, Turkey, focusing on two high-pollution episodes in January 2002. To better maintain large scale features, model simulations were nudged to reanalysis for this application. Using a semi-idealized approach, it was shown that much of the pollution that affected Istanbul during these events may have come from other highly polluted cities located upstream, rather than just local emission sources. Pollutants from upstream sources were trapped in the boundary layer by statically stable low-level conditions and efficient transport to Istanbul was supported by strong northwesterly flow near the surface. The second application involves the transport of dust from the Sahara Desert to the Atlantic Ocean, and the potential role of this dust and the dry, warm Saharan Air Layer (SAL) in the genesis and development of Tropical Storm Chantal in 2001. No nudging was applied to this case study since it may degrade small scale features, which were important to dust saltation. The dust uplifting and transport during the earlier period of Chantal's life cycle were simulated to show a potential link between Sahara dust and Chantal's evolution. Results show strong evidence that Chantal started interacting with SAL and dust at a very early stage of storm development after propagating into the eastern Atlantic Ocean. Moreover, it was found that the peak of the averaged surface dust flux occurred in the early morning right before the mixed boundary layer developed, and the mechanism of dust uptake for this event, nocturnal low-level jets, was different from those previously documented.

**Citation:** Chen, S.-H., J. Dudhia, J. S. Kain, T. Kindap, and E. Tan (2008), Development of the online MM5 tracer model and its applications to air pollution episodes in Istanbul, Turkey and Sahara dust transport, *J. Geophys. Res.*, *113*, D11203, doi:10.1029/2007JD009244.

### 1. Introduction

[2] Air quality has become an important issue to society since it strongly affects human health and visibility. Although poor air quality is often attributed to local emission of pollutants, the local air quality can be impacted

by remote emission sources as well. Therefore it is important to take into account the transport effect when considering new policies aimed at improving air quality [e.g., Kubilay *et al.*, 2000; Westphal *et al.*, 1988; Bergametti *et al.*, 1989; Nickovic and Dobricic, 1996; Kallos *et al.*, 1998; Rodriguez *et al.*, 2001; Kindap *et al.*, 2006]. Moreover, pollutants, in particular those suspended in the air for a long time and traveling long distances, can modify weather systems and climate through radiation and cloud microphysics processes. To better understand the influence of pollutants on weather and climate, the origins and transport of pollutants should be identified and their impacts should be investigated.

[3] In pollutant transport or air quality studies, the off-line approach, which runs an air pollution model and a meteorological model separately, is commonly used [Reiff *et al.*, 1986; Karyampudi *et al.*, 1999; Seigneur *et al.*, 2003; Lee *et al.*, 2004; Hogrefe *et al.*, 2004; Jimenez *et al.*, 2005; Kindap *et al.*, 2006]. This approach is less than ideal because of inconsistencies between the air pollution (or trajectory) model and the meteorological model. For example, the

<sup>1</sup>Department of Land, Air, and Water Resources, University of California, Davis, California, USA.

<sup>2</sup>Department of Atmospheric Science, National Central University, Chung-Li, Taiwan.

<sup>3</sup>Mesoscale and Microscale Meteorology Division/NCAR, Boulder, Colorado, USA.

<sup>4</sup>National Severe Storms Laboratory, National Weather Center, Norman, Oklahoma, USA.

<sup>5</sup>Eurasia Institute of Earth Sciences, Istanbul Technical University, Istanbul, Turkey.

<sup>6</sup>Department of Civil and Environmental Engineering, University of California, Davis, California, USA.

<sup>7</sup>Department of Meteorological Engineering, Istanbul Technical University, Istanbul, Turkey.

two models might use different parameterization schemes (e.g., boundary layer turbulence mixing and cumulus convection). They might also use different temporal and spatial resolutions [Seaman, 2000], and in many applications of air pollution models the meteorological fields are updated quite infrequently (typically on the order of hours) due to storage limitations. The resulting temporal interpolation between update times can introduce significant errors in transport computations, especially over the areas where boundary layer height and/or wind vary significantly with time. Such errors can make it difficult to arrive at sound policy decisions or to assess the impact of pollutants on weather and climate. Therefore an online approach in studying pollutant transport and air quality has become increasingly popular [Nickovic and Dobricic, 1996; Liu et al., 2003; Perez et al., 2006; Kallos et al., 2006].

[4] Herein, an online approach, based on the fifth-generation NCAR/Penn State Mesoscale Model (MM5; Grell et al. [1995]), is presented. The new online tracer model is called MM5T. The potential utility of this model is demonstrated by simulating two high-pollution episodes that occurred in Istanbul, Turkey during January 2002 and one case of Saharan dust transport that was associated with the formation and development of the tropical storm Chantal in 2001.

[5] The Istanbul events occurred on 7–8 and 10–12 January 2002. During these events, the atmospheric circulation over central Europe was dominated by a cold-core surface anticyclone, a climatologically favored feature during the cold season [Kallos et al., 1998]. Air trajectories associated with this anticyclone were consistent with the transport of high concentrations of PM<sub>10</sub> (particulate matter with diameter <10  $\mu\text{m}$ ) from upstream emission sources, and its characteristic high static stability at the top of the boundary layer inhibited mixing with the free troposphere. Therefore we hypothesize that PM<sub>10</sub> transported from upstream sources was partially responsible for these two pollution events in Istanbul.

[6] Kindap et al. [2006] studied both of these events using an off-line air pollution model. They used meteorological data from MM5, which has been often used to drive such models [Seigneur et al., 2003; Lee et al., 2004; Hogrefe et al., 2004; Jimenez et al., 2005]. Their sensitivity simulations showed that long-range pollutant transport from upstream sources could have been responsible for a significant fraction of the PM<sub>10</sub> concentrations observed in Istanbul. However, their off-line approach required several approximations that could be avoided with an online model. In this study, the newly developed MM5T is used to provide a more accurate assessment of the relative contributions of local emissions and long-range transport for these two events.

[7] The study of Saharan dust transport was motivated by recent studies showing that the Saharan Air Layer (SAL), which is an extended warm, dry, and potentially dusty air from the Sahara Desert to the Atlantic Ocean, influences easterly wave disturbances and Tropical Cyclone (TC) activity [Karyampudi and Carlson, 1988; Karyampudi et al., 1999; Karyampudi and Pierce, 2002; Dunion and Velden, 2004; Wu et al., 2006]. The SAL can extend from 850 hPa to 500 hPa over the Atlantic Ocean from the Sahara Desert to the West Indies and the United States during late

spring to early fall [Prospero and Carlson, 1972; Dunion and Velden, 2004]. Two to three decades ago, our understanding of TC activity was limited due to a lack of observations and weak balance flow in the tropics. After satellite data became available and many field experiments were conducted, the influence of the SAL on TC activity has been gradually revealed, but many unknowns still remain. Karyampudi and Pierce [2002] and Dunion and Velden [2004] found that the genesis and development of TCs over the Atlantic Ocean could be enhanced or suppressed by the SAL. Wong and Dessler [2005] also illustrated that deep convective activity was suppressed by the SAL raising the levels of lifting condensation and free convection and boosting the energetic barrier to convection in the North Atlantic. In general, the influence of the SAL on TC activity can be through a variety of processes, such as the entrainment of dry, stable air into the storm which promotes evaporatively driven downdrafts in TCs; the maintenance of a midlevel easterly jet located around 600–700 hPa due to warm SAL air at the north of the jet which increases vertical shear; or the enhancement of pre-existing trade wind inversions in the Atlantic which stabilizes the atmosphere [Dunion and Velden, 2004].

[8] In addition to the dry, warm SAL, Sahara dust, if there is any, can have an impact on TC activity through radiation and cloud microphysical processes. Dunion and Velden [2004] documented that SAL strongly influenced the activity of the tropical storm Chantal (2001), which consequently struggled to maintain its intensity. It was suspected that not only the dry, stable Saharan air but also the dust had an influence on this storm's genesis and development.

[9] Satellite data and ground-based measurements have been successfully used to map Saharan dust sources [Bergametti et al., 1989; Ginoux et al., 2001; Prospero et al., 2002]. Prospero et al. [2002] applied NASA's Earth Probe/Total Ozone Mapping Spectrometer (EP-TOMS) satellite aerosol index data to investigate the global distribution of major atmospheric dust sources and identified a dust belt extending from the west coast of North Africa, over the Middle East, and Central and South Asia, to China. Studies also found that dust sources might be primarily from a few preferential regions, such as topographic depressions [Ginoux et al., 2001; Prospero et al., 2002]. For example, Bodele Depression, located at the southern edge of the Sahara Desert, has been identified as the most intense dust source in the world [Prospero et al., 2002; Washington et al., 2003]. In addition to identifying dust sources, TOMS satellite data have been used for studying dust propagation and for validation of simulated/forecasted long-range dust transport [Chin et al., 2002, 2003; Kinne et al., 2003; Wang, 2007].

[10] A few online dust models were also developed based on existing mesoscale models as in this study. For example, SKIRON, which was developed based on the Eta model at University of Athens [Kallos et al., 1997, 2006], has been running for dust and weather forecasting over the Mediterranean region since 1998 with a resolution of a quarter degree [Kishcha et al., 2007]. The Dust Regional Atmospheric Modeling (DREAM; Nickovic et al. [2001]) system, which was also based on Eta, has been regularly predicting dust over the Mediterranean region with a resolution of 50 km [Perez et al., 2006]. The dust compo-

ment was implemented into the U.S. Navy's operational Coupled Ocean/Atmospheric Mesoscale Prediction System (COAMPS) [Liu *et al.*, 2003] and was used for dust storm forecasts over the Iraq region with three nested domains at resolutions of 9, 27, and 81 km in March and April 2003 [Liu *et al.*, 2007].

[11] In our second application, the MM5T was used to investigate Sahara dust saltation and transport during the early period of the Chantal life cycle with a comparable resolution to those mentioned above. The impact of dust on storm activity is left for future work. The mechanisms of dust saltation over the desert and the characteristics of atmospheric flow associated with the SAL are also discussed and documented.

[12] This paper is organized as follows. The overview of the numerical model development is given in section 2. The application of MM5T to air pollution episodes in Istanbul, Turkey is demonstrated in section 3, while the application to Sahara dust transport is presented in section 4. Concluding remarks are given at the end.

## 2. A Brief Description of the Development of an Online Tracer Model

[13] Using the MM5 version 3.6, an online tracer model (MM5T) was developed to study the long-range transport of aerosols. MM5 uses the Arakawa B grid in the horizontal dimensions. In the vertical, a terrain-following height coordinate is used, and the vertical velocity is staggered vertically from other variables. In addition to the governing equations used in the MM5 model, a continuity equation describing the amount of tracers present ( $C$ ) was introduced in MM5T and is written as:

$$\frac{\partial C}{\partial t} = -\bar{V} \bullet \nabla C + C_{\text{pbl}} + C_{\text{cov}} + S_C + E_C, \quad (1)$$

where  $\bar{V}$  is the three-dimensional wind vector. The transport effects due to advection ( $-\bar{V} \bullet \nabla C$ ), boundary layer mixing ( $C_{\text{pbl}}$ ), subgrid cumulus convective mixing ( $C_{\text{cov}}$ ), and sedimentation ( $S_C$ ) were taken into account. In this simple version, chemical reactions are excluded and wet deposition is ignored as well. Therefore in the whole system the only source term is the emission ( $E_C$ ) from the surface and the only sink term is the dry deposition to the surface due to sedimentation. In this study, the emission rate,  $E_C$ , and the sedimentation rate,  $S_C$ , were specified according to the different applications, as discussed later. For simplicity, the impact of aerosols on the radiation budget, including scattering and absorbing, was also ignored.

[14] The Medium Range Forecast (MRF) boundary layer scheme [Hong and Pan, 1996], which includes local and nonlocal mixing, and the Kain-Fritsch cumulus convection scheme [Kain, 2004], which includes deep and shallow convection, were chosen and modified to account for the tracer mixing effects. With this configuration, tracer evolution is treated essentially the same as that of any other scalar in the model, except that it has unique source and sink terms. This online approach can avoid the temporal interpolation errors that inherently limit the accuracy of off-line calculations of pollutant transport and diffusion.

[15] In MM5T, tracers were designed as a 4D array which makes it easier to vary the number of tracers. For air pollution episodes in Istanbul, Turkey, the same type of pollutants emitted from different locations on different dates were tracked individually using different tracers. Therefore the source and date of pollutants from upstream can be identified more accurately and precisely. This detailed information can be important when policy decisions are made to improve air quality. For dust simulations, different types of dust emitted from northern Africa and the north-western Middle East were tracked so that the dust types that potentially influence the genesis and development of tropical storms could be identified. This information is important to physical processes in numerical models, which will be considered in future work.

## 3. Application of the MM5T to Air Pollution Episodes in Istanbul, Turkey

[16] Figure 1 shows the time series of observed PM10 concentration at Umraniye, Uskudar, Besiktas, and Sarachane stations in Istanbul from 5 to 12 January 2002. Two high PM10 episodes were consistently recorded in these stations during 7–8 (e.g., 48–72 h) and 10–12 (120–168 h) January 2002. While pollutants can be emitted locally, long-range transport is a possible contributor to high pollution events when weather conditions are favorable. The developed MM5T was used to investigate the possibility that pollutants were transported from other cities upstream of Istanbul, Turkey.

### 3.1. Experiment Design

[17] For MM5T simulations, a single domain with grid-spacing of 30 km covering the entire European continent and nearby seas was configured. It had  $227 \times 176 \times 38$  grid points in the east-west, north-south, and vertical directions, respectively. The Lambert projection was used. The vertical resolution was stretched from approximate 20 m close to the surface and gradually decreased to 1400 m close to the model top. In addition to the MRF boundary layer parameterization and the Kain-Fritsch convection scheme, the RRTM (Rapid Radiative Transfer Model) radiation scheme [Mlawer *et al.*, 1997] and simple ice microphysics scheme [Dudhia, 1989] were chosen. A time step of 90 s was used.

[18] Two tracer simulations were conducted, experiment 1 (EXP1) and experiment 2 (EXP2), corresponding to the two peak events of PM10 concentration in Istanbul, 7–8 and 10–12 January 2002. Specifically, the model was integrated from 5 January 0000 UTC to 8 January 0000 UTC for EXP1 and from 8 January 0000 UTC to 11 January 0000 UTC for EXP2. For this case study, the National Centers for Environmental Prediction (NCEP) Global Data Assimilation System (GDAS) 6 hourly reanalysis data (with  $2.5^\circ$  latitude/longitude resolution) were used for MM5T boundary and initial conditions. In addition, both simulations were nudged with GDAS reanalysis (i.e., using four dimensional data assimilation) to keep the model on track because synoptic scale patterns are important to long range pollutant transport.

[19] The emission source term,  $E_C$ , was represented by an idealized form based on the emission module developed by Kindap *et al.* [2006]. This module can be used to downscale

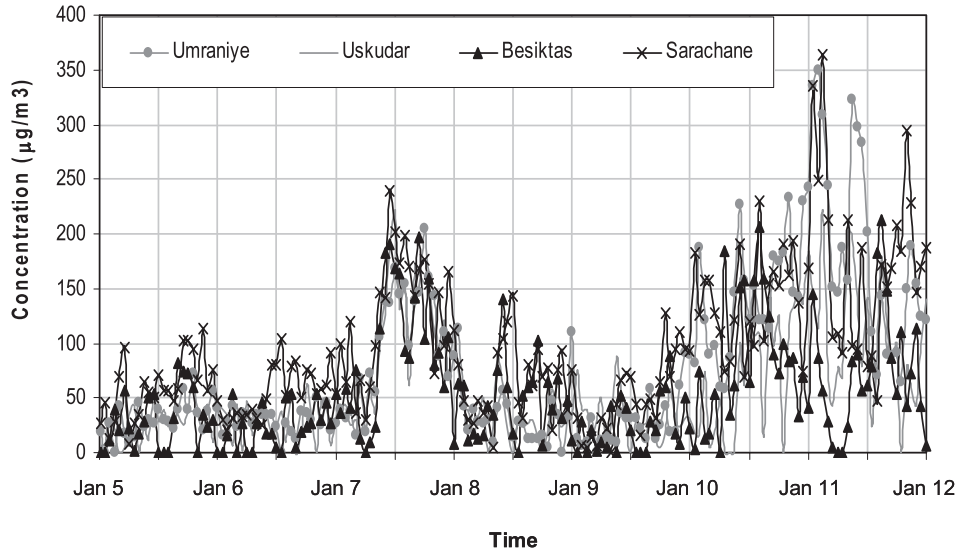


**Figure 1.** Time series of measured PM10 concentrations at Umraniye, Uskudar, Besiktas, and Sarachane observation stations in Istanbul from 0000 UTC 5 January to 0000 UTC 12 January 2002 (Courtesy Kindap *et al.* [2006]).

in time from annual EMEP (the European Monitoring and Evaluation Programme) emission data to hourly rates. The EMEP inventory is the best emission inventory, with data (main pollutants including particulate matter) available as annual totals for each European country [Kindap *et al.*, 2006]. The maximum emission rate from their module occurs at about 5 p.m. local time. This emission cycle was mimicked in our tracer simulations and tracers were released from the surface into the lowest model layer over a daily cycle as shown in Figure 2, with a maximum of about  $3.3 \times 10^{-3}$  unit  $s^{-1}$  at 5 p.m. local time. The sedimentation term ( $kg\ kg^{-1}\ s^{-1}$ ) was calculated using the formula:

$$S_c = \frac{1}{\rho} \times \frac{d(\rho C V_T)}{dz}, \quad (2)$$

where  $\rho$  and  $V_T$  are the full density and terminal velocity ( $m\ s^{-1}$ ), respectively, and the terminal velocity is simply calculated using  $V_T = 0.01 \times C^{0.2}$ , where the mixing ratio of the tracer ( $C$ ) is in a unit of  $kg\ kg^{-1}$ .

[20] Since this study was designed to demonstrate the potential utility of using MM5T to track pollutants from their origins, simulated emission sources were limited to a few potential locations in Europe. In particular, Warsaw, Silesia, and Krakow in Poland; Kiev in Ukraine; Moscow in Russia; Sofia and Plovdiv in Bulgaria; and Bucharest in Romania were selected. These cities were chosen because they were potentially significant local sources of anthropogenic pollutants and they were positioned upstream of Istanbul on the dates in question. It was assumed that the area of tracer emission in each city had a radius of 100 km, and the emission was independent of location within the designated emitting area. For simplicity, we further assumed

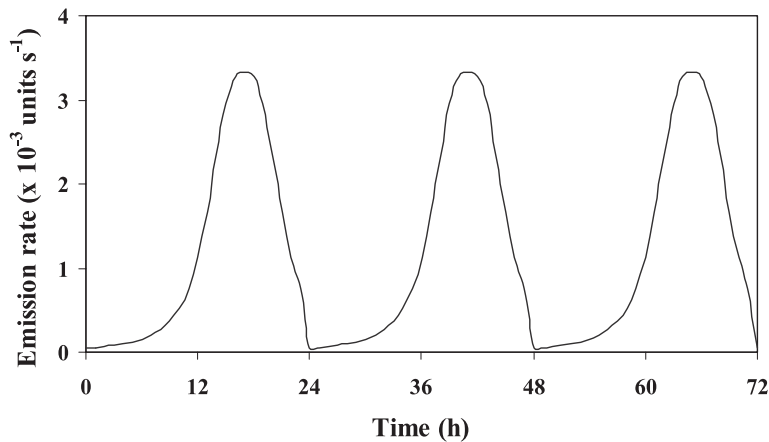


**Figure 2.** Idealized emission rate that was used for MM5T simulations.

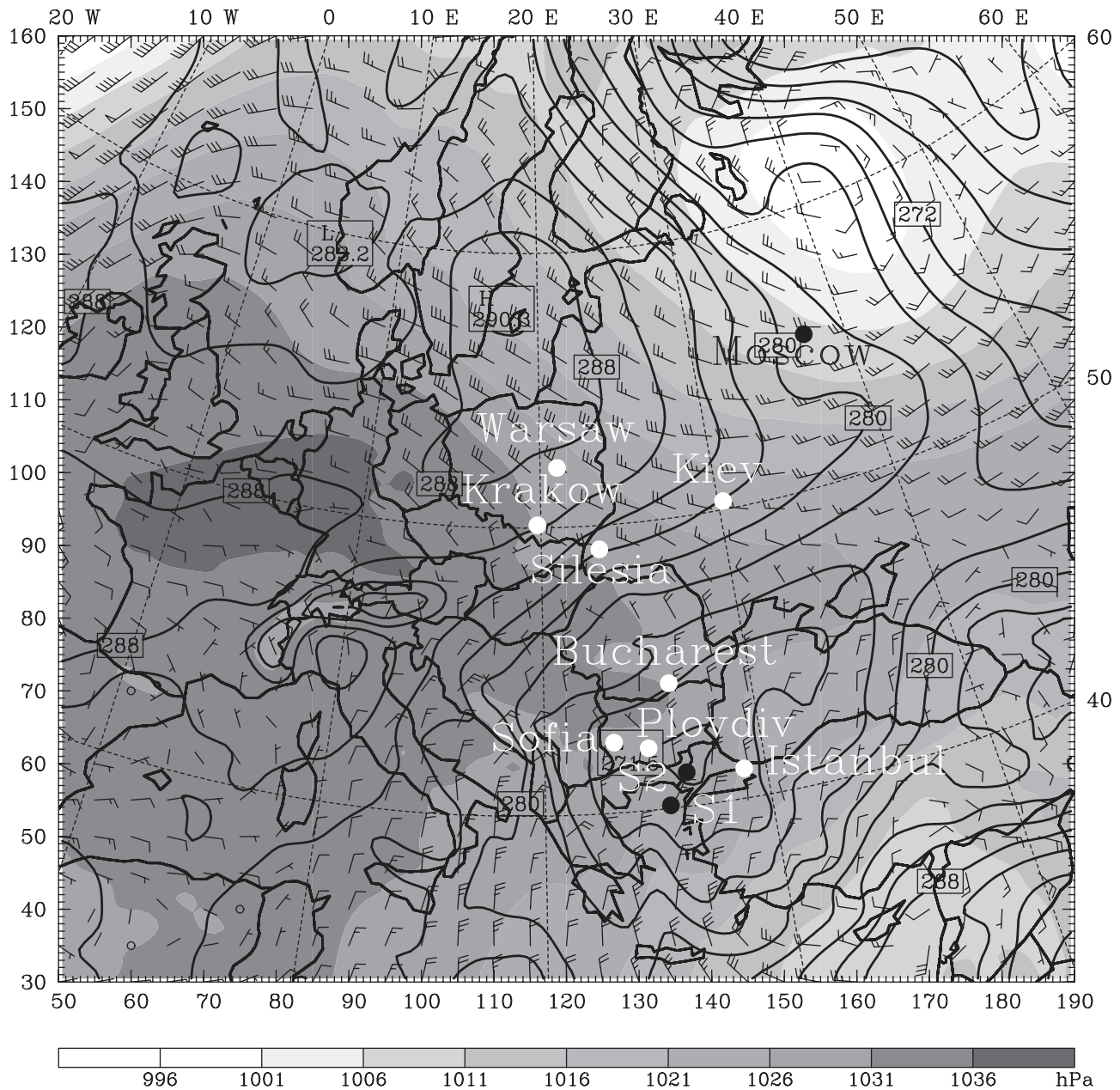


**Figure 3.** Twenty-four-hour simulation from EXP1, showing sea level pressure (shaded; hPa), 1.5-km potential temperature (solid lines; K), and 950-mb wind vectors at 0000 UTC 6 January 2002. Marked cities were used for tracer experiments in this study, except S1 (Gokceada) and S2 (Uzunkopru) which are the locations for plots in Figures 4a and 4b, respectively.

that the same emission function and magnitude were used and all pollutants were injected into the first model layer near the surface for every source location. It is noted that, in reality, the emission rate can be very different from one city to another and pollutants can be injected into different model layers, which may influence simulated pollutant transport. It is feasible to incorporate an emission module with more realistic emission data into the MM5T model, but we leave it for future work.

[21] To further investigate the transport characteristics, tracers from the same city but different days (i.e., 0000 UTC to 0000 UTC next day) were tracked separately (i.e., monitored using different tracers). Note that tracers released

from Silesia and Krakow were not distinguished because of their similar pollutant characteristics.

### 3.2. Results and Discussions

[22] After 24 h of integration in EXP1, a synoptic-scale circulation pattern that favors low-level pollutant transport from the selected locations into Turkey was quite evident (Figure 3). Specifically, a surface high-pressure center was positioned over central Europe while a surface low was located over western Russia. The pressure gradient between these two centers induced strong boundary layer flow into Turkey from the north-northwest, creating a mechanism for the fast transport of PM<sub>10</sub> from upstream cities to Istanbul.

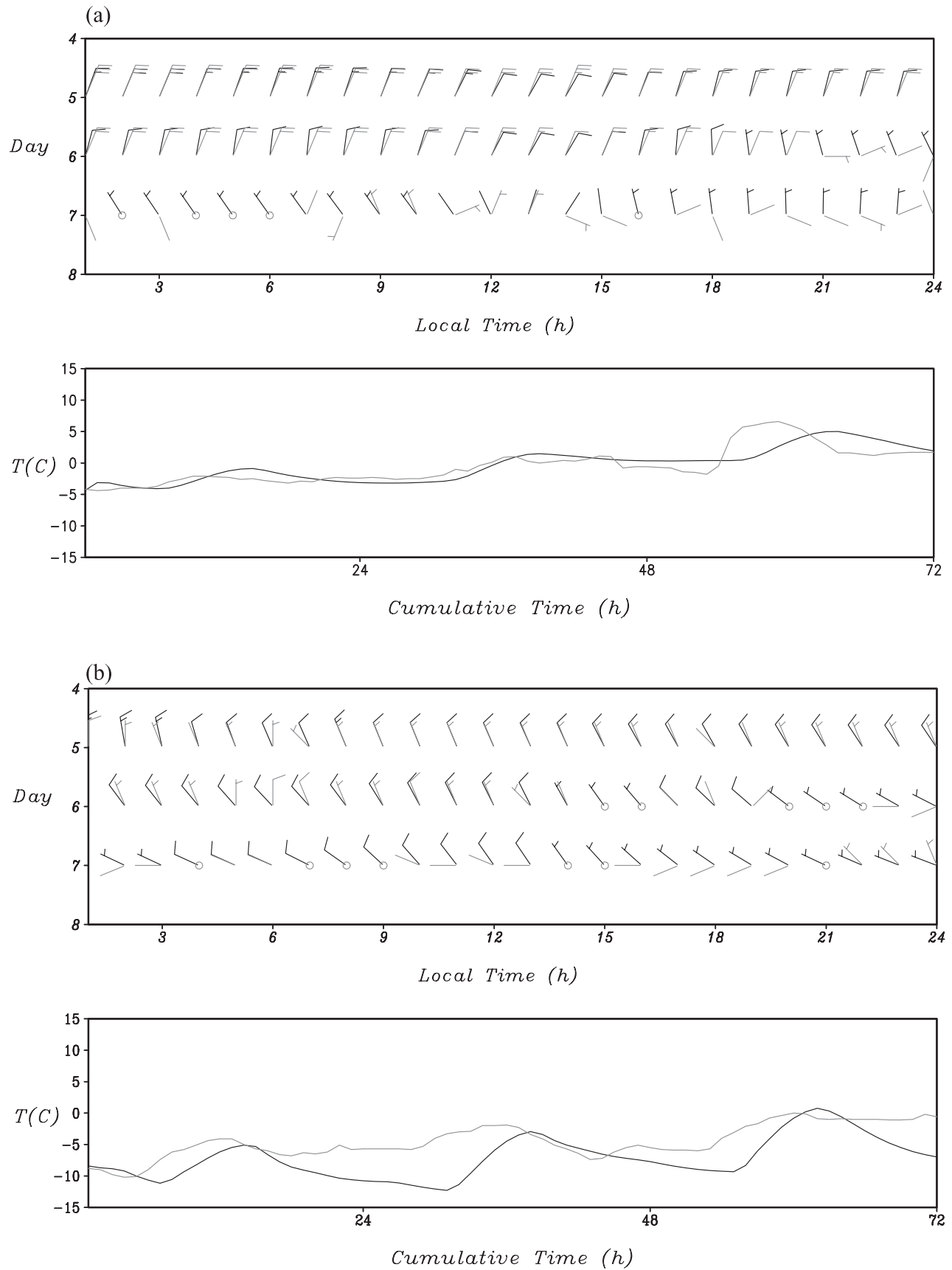


**Figure 4.** Observed (gray lines) and 72-h MM5T simulated (black lines) 10-m winds (knots; a full barb equals 10 knots and a half barb equals 5 knots) and 2-m temperature ( $^{\circ}C$ ) for (a) Gokceada (S1 in Figure 3) and (b) Uzunkopru (S2 in Figure 3) from EXP1 at stations near Istanbul.

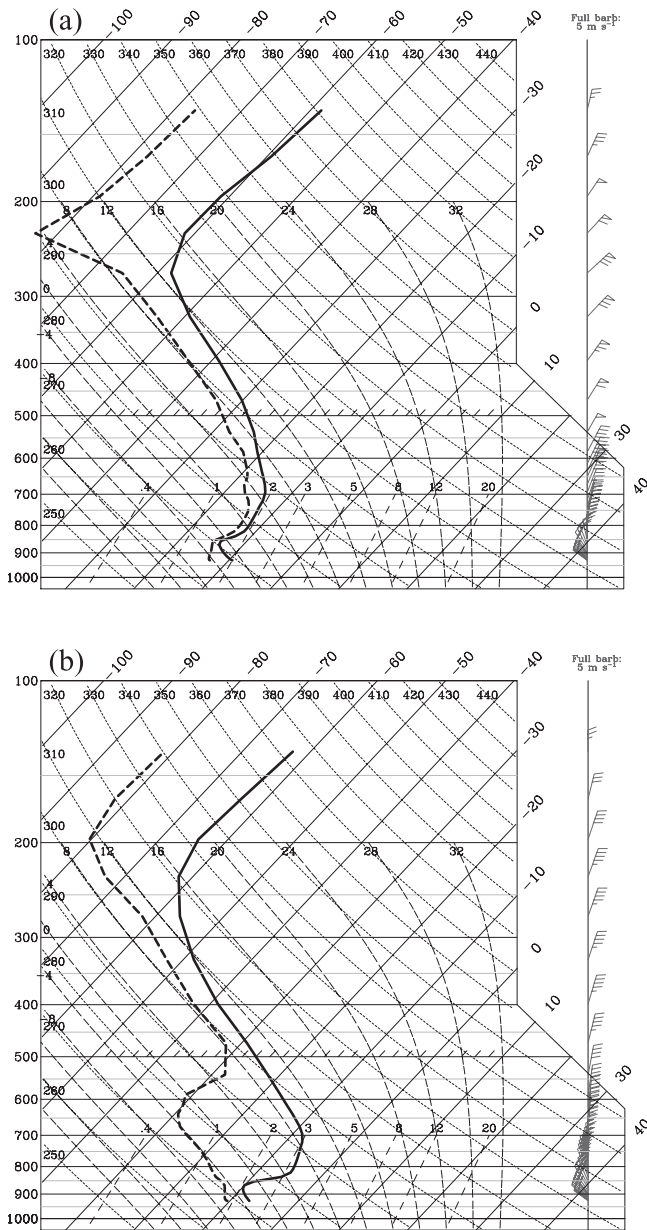


**Figure 5.** Vertical sounding at the location S1 in Figure 6a (white dot) after (a) a 12-h (i.e., 1200 UTC 5 January 2002) and (b) a 36-h simulation (i.e., 1200 UTC 6 January 2002) from EXP1.

The model-simulated wind fields were quite realistic in the vicinity of Istanbul during the first two days of the simulation, though the consistency was not as good on the third day, when observed winds were relatively calm (Figure 4), which is a common problem for numerical model forecasts. The model simulated the low-level temperatures skillfully for the slow variation of temperature at Gokceada (sky was overcast). The diurnal oscillation at Uzunkopru, however, was not simulated well due to the nudging of GDAS reanalysis. While the use of reanalysis data can help maintain large scale features better, it may unfortunately degrade model performance on shorter time-scales, such as the diurnal cycle. For EXP1, a surface cold front passed

through the area during the first 12 h (Figure 5a) followed by subsidence from the high pressure system (Figure 5b), leaving in its wake an exceptionally strong stable layer at the top of the boundary layer. The stable layer suppressed vertical mixing, apparently allowing pollutants to remain

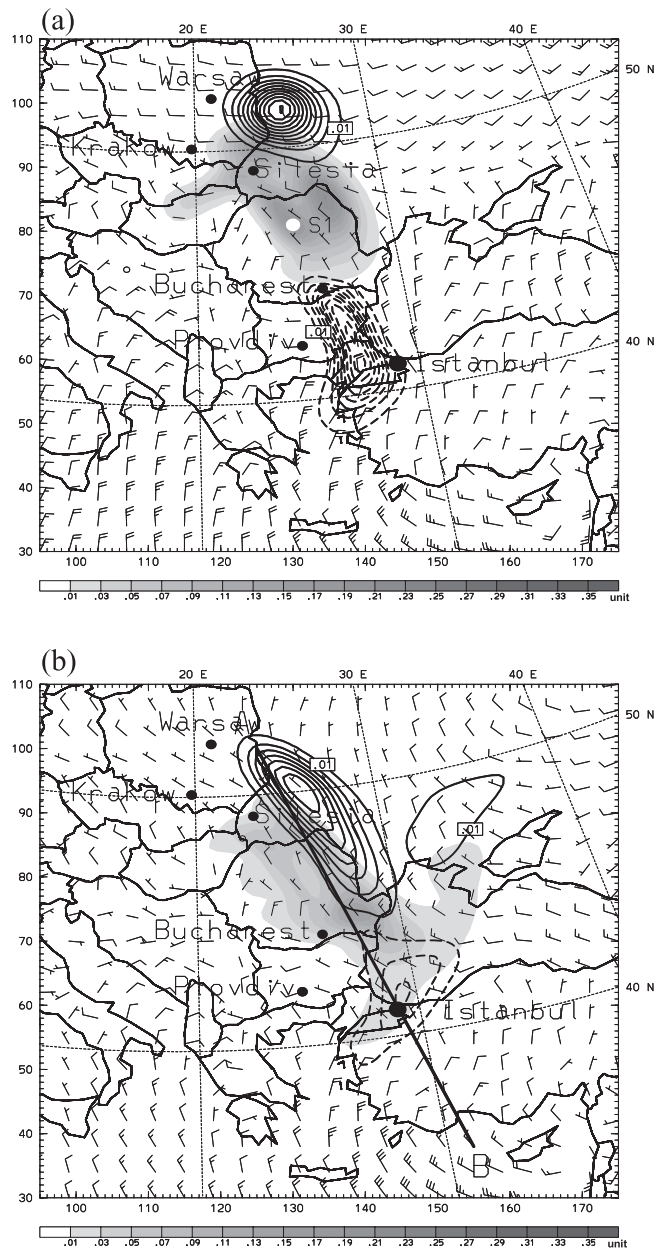


**Figure 6.** Snapshot of simulated tracers and wind vectors at the 100-m height at (a) 24-h and (b) 54-h simulation from EXP1. Only the three most significant amounts of tracers, i.e., from Bucharest (dashed lines), Silesia and Krakow (shaded), and Warsaw (solid lines) that contributed pollutants to Istanbul are plotted. Tracers in Figure 6a were released during the first day. In Figure 6b tracer from Bucharest (dashed lines) was released during the 2nd day and tracers from Silesia and Krakow (shaded) and Warsaw (solid lines) were released during the first 2 d. The interval is 0.02 units. S1 (white dot) in Figure 6a is the location for the plot of the vertical sounding in Figure 5.

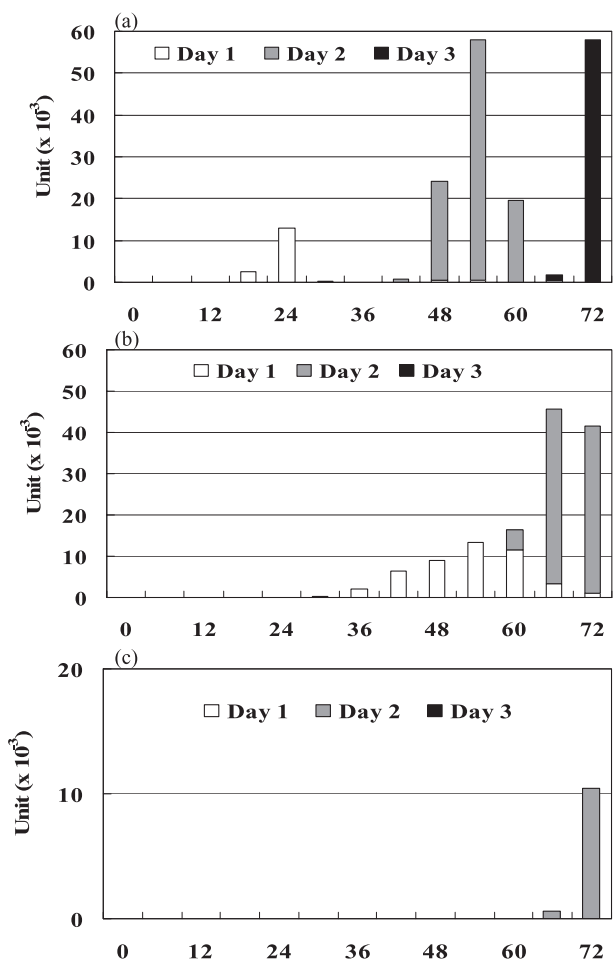


**Figure 7.** Time series of simulated tracer collected at 100-m height in Istanbul. Tracers were emitted from (a) Bucharest (Romania), (b) Silesia and Krakow (Poland), and (c) Warsaw (Poland) for EXP1. White, gray, and black colors indicate tracers that were emitted on day 1 (0–24 h), day 2 (24–48 h), and day 3 (48–72 h) from each particular city. Note that the plotted ranges of the y axis are different.

concentrated near the surface. Note that the upper-level northeasterly wind in Figure 5 is due to the upper-level northeast-southwest orientation of the trough.

[23] Meteorological results from EXP2 were comparable to those from EXP1. Therefore we conclude that the MM5T produced sufficiently realistic meteorological data to compute estimates of tracer transport for the Istanbul case study.

[24] The snapshot of simulated tracer (pollutant) transport from the three most significant source cities to Istanbul for EXP1 is plotted in Figure 6. For the first simulation period (0000 UTC 5 January to 0000 UTC 8 January), although pollution released from Bucharest in Romania on the first day reached Istanbul, low-level trajectories appear to have carried most of the Bucharest plume to the west of the city (dashed lines in Figure 6a) and it made a relatively small contribution in Istanbul (white bars in Figure 7a). However, pollution released in Bucharest on the second day began to reach Istanbul at 0000 UTC 7 January (after about 1 d

transport time) and had a maximum impact on the city at 0600 UTC 7 January, when the peak of the pollutant plume passed through the city (dashed lines in Figure 6b and gray bars in Figure 7a). Since Bucharest is close to Istanbul, pollutants released from there on the third day reached Istanbul before the end of simulations.

[25] Silesia and Krakow in Poland are relatively far away from Istanbul, yet pollution released from both cities on the first day reached Istanbul after about 36 h of transport (by

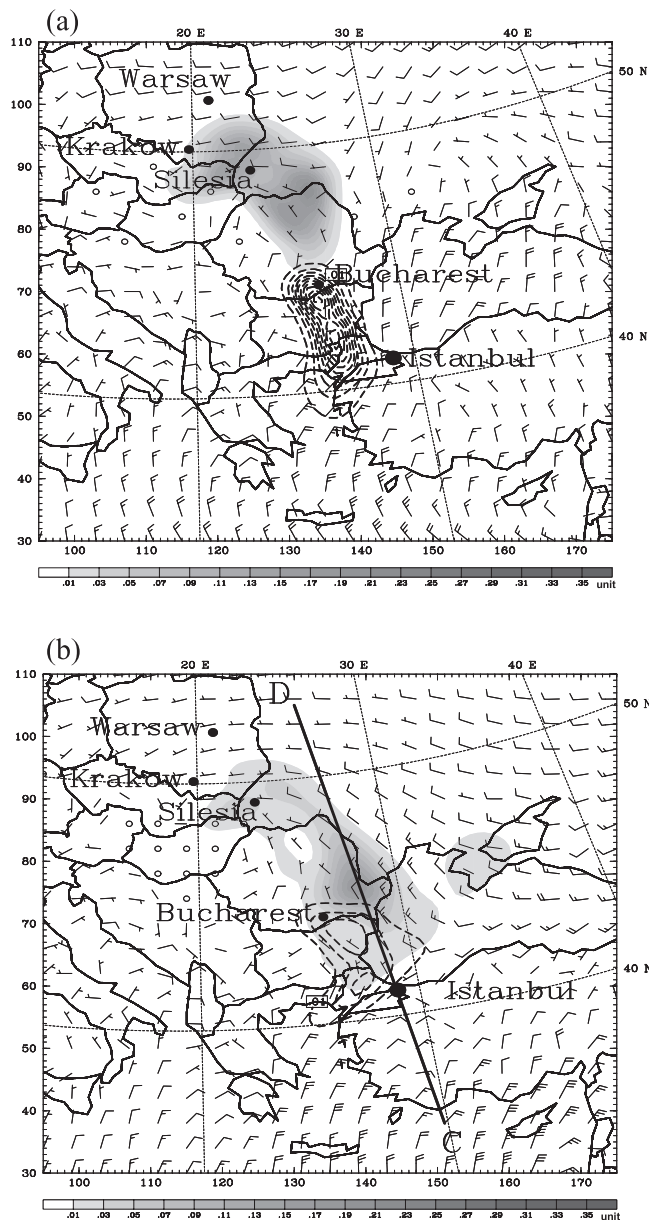


**Figure 8.** Snapshot of simulated tracers and wind vectors at the 100-m height at (a) 24-h and (b) 54-h simulation from EXP2. Only the two most significant amounts of tracers, i.e., from Bucharest (dashed lines) and Silesia and Krakow (shaded), that contributed pollutants to Istanbul are plotted. Tracers in Figure 8a were released during the first day. In Figure 8b tracer from Bucharest (dashed lines) was released during the 2nd day and tracers from Silesia and Krakow (shaded) were released during the first 2 days.

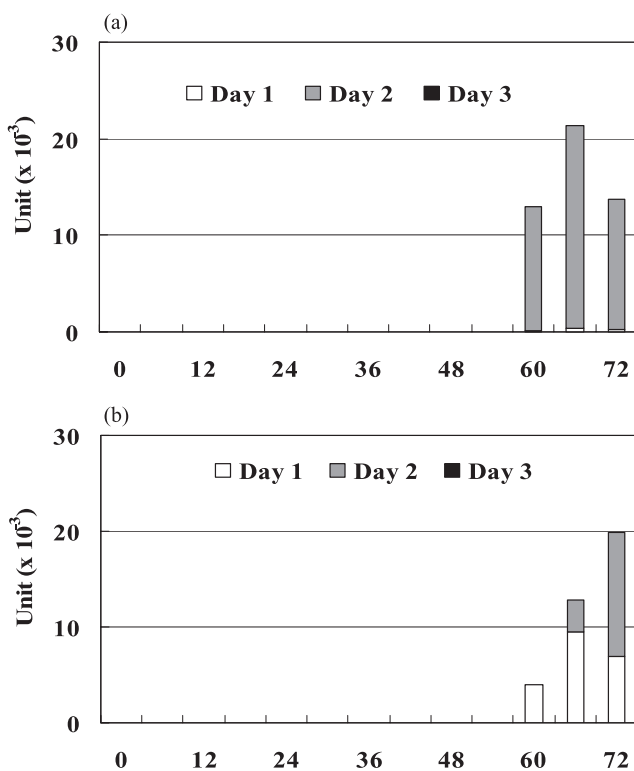


**Figure 9.** Time series of simulated tracer collected at 100-m height in Istanbul. Tracers were emitted from (a) Bucharest (Romania) and (b) Silesia and Krakow (Poland) for EXP2. White, gray, and black colors indicate tracers that were emitted on day 1 (0–24 h), day 2 (24–48 h), and day 3 (48–72 h) from that particular city.

1200 UTC 6 January) and their influence on the city lasted for one and a half days (shading in Figure 6b and white bars in Figure 7b). Silesia's and Krakow's pollutants from the second day reached the city as well, arriving at around 1200 UTC 7 January (i.e., 36-h transport) with a higher concentration than the first day's plume (shading in Figure 6b and gray bars in Figure 7b). Though it took more time to transport to Istanbul, the peak amount of pollutants from Silesia and Krakow reaching the city was about 78.6% of that from Bucharest.

[26] Because of the location of the low pressure center, pollution released the first day from Warsaw, Poland, which is farther away from Istanbul, slowly moved east-southeastward and never arrived at Istanbul (Figure 6a). As the low pressure system over western Russia gradually moved southeastward, a favorable condition was provided for the 2nd day Warsaw plume to move toward Istanbul (Figure 6b). After a 42-h propagation the plume reached Istanbul before the end of the simulation; however, the concentration was significantly diluted (gray bars in Figure 7c). It is interesting to see that these most significant source cities had the maximum amount (or the second maximum amount for Bucharest) of pollution that arrived in Istanbul on the third day when the high pollution episode occurred. Other selected cities such as Kiev, Sofia, and Plovdiv contributed almost no pollutants to Istanbul in the first event due to the directions of low-level winds.

[27] Results from EXP2 (Figures 8 and 9) were very similar to those from EXP1 (Figures 6 and 7). However, pollutants from Warsaw in Poland did not reach Istanbul. Therefore only the results from Bucharest in Romania and Silesia and Krakow in Poland are plotted. For those plotted tracers, the pollutant amount transported to Istanbul was smaller and the impact duration on the city was shorter (see Figures 7 and 9) compared with EXP1. The transport times of pollutants from different cities were longer than those from EXP1. The contribution of long-range transport from Bucharest, Romania was still the highest (Figure 9). Pollution from Silesia and Krakow, Poland was comparable to that from Bucharest (recall that the same magnitude of emissions was used for all cities). In this event, the high-pressure system over central Europe in EXP1 moved eastward and was the primary contributor to the favorable environment configuration for long-range transport.

[28] As mentioned above, vertical dispersion of boundary layer pollutants was suppressed by strong static stability at the top of the boundary layer. A vertical cross section from EXP1 shows that the pollutant plumes released from Bucharest, Silesia and Krakow, and Warsaw were trapped below 1.2 km as they were advected toward Istanbul (Figure 10a). Similar results were obtained for EXP2 (Figure 10b), which took place during a period of comparably strong boundary layer capping. Note that the topography in this area is very complex (Figure 10) and wind directions and magnitudes can vary with time significantly.

[29] While MM5T indicated that remote sources of pollution made relatively small contributions to the total pollutant concentration in Istanbul during most of the peak local emission times (Figure 11), a contribution of 3.3% from long-range transport could occur for the highest peak in EXP1 (e.g., the 60 h time in Figure 11a). The contribution could increase to  $\sim 20$ –25% at the off-peak times when pollution concentrations were still relatively high in Istanbul, such as 54 h and 66 h in EXP1. In contrast, when local emission was relatively small, the simulation results showed that pollutants from upstream could have dominated the local air quality (e.g., the 72 h time in EXP1). It is worth pointing out that while some uncertainties exist in the MM5T calculation, the value of 3.3% from EXP1 is probably conservative since only limited cities were examined in this demonstration. For EXP2, the contribution of the long-range transport during the peak times was smaller than that of EXP1 (Figures 11a versus 11b).

[30] Although idealized emission was used, the time variation of simulated concentration from both experiments (Figure 11) was qualitatively similar to the observed concentrations shown in Figure 1. The maximum occurred at the third day of each experiment as observed when the winds were relatively weak.

#### 4. Application of the MM5T to Sahara Dust Transport

[31] Tropical Storm Chantal (2001), a poorly organized storm, developed from a tropical easterly wave over the coast of Africa and propagated into the eastern Atlantic on 11 August 2001. The convective system weakened after propagating over the ocean and redeveloped by 13 August. Chantal became a tropical storm early on the 14th and

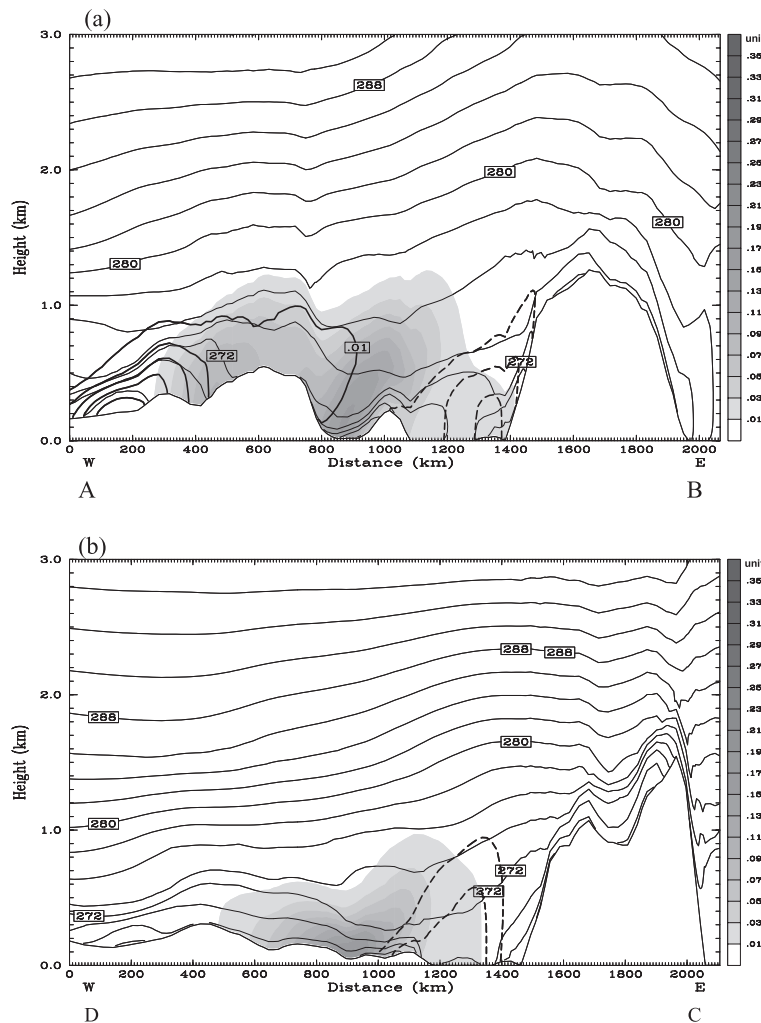


**Figure 10.** Vertical cross-sections of 54-h simulated tracers below 3 km along the lines AB and CD in Figures 6b and 8b for (a) EXP1 and (b) EXP2, respectively. In Figure 10a Bucharest (dashed lines), Silesia and Krakow (shaded), and Warsaw (solid lines) are plotted. In Figure 10b Bucharest (dashed lines) and Silesia and Krakow (shaded) are plotted.

became a tropical depression later the same day. The storm degenerated into a wave disturbance again near 1200 UTC on the 16th at the time when the storm's moving speed increased to  $15 \text{ m s}^{-1}$ . Chantal slightly regained strength late on the 18th after the moving speed reduced to  $10 \text{ m s}^{-1}$ . The storm made landfall in Belize and the Yucatan Peninsula, Mexico on the 20th and diminished two days afterward, failing to become a hurricane. Details about Chantal are available in a preliminary report at [www.nhc.noaa.gov/2001chantal.html](http://www.nhc.noaa.gov/2001chantal.html).

[32] Figure 12 shows a 6-d time series of integrated aerosols from the TOMS satellite aerosol index data [McPeters *et al.*, 2000] over northern Africa and the Atlantic Ocean. A significant amount of dust was uplifted into the atmosphere during 9–10 August 2001. When Chantal was still a wave disturbance propagating into the eastern Atlantic on 11 August, the dust was also transported into the eastern Atlantic Ocean through Western Sahara and Mauritania and then continued propagating into the central Atlantic Ocean. As the dust plume and the easterly wave disturbance propagated toward the central Atlantic, we

suspected that not only dry, stable Saharan air but also Sahara dust had an influence on Chantal's genesis and development. In this study, the dust origin, saltation, and transport were studied using the developed MM5T to show a potential link between Sahara dust and Chantal's activity in the eastern Atlantic Ocean, while the impact of dust on hurricane development through physical processes will be left for future work.

#### 4.1. Experiment Design

[33] As in the previous experiment, a single domain with grid-spacing of 30 km was configured and the same physics schemes were chosen. The grid points were  $380 \times 230 \times 38$  in the east-west, north-south, and vertical directions, respectively, and the domain covered northern Africa, northwestern Middle East, and the Atlantic Ocean. Also as in the first case study, the Lambert projection was applied and similar vertical grid spacing was used. In this Sahara dust simulation, an accurate representation of the diurnal cycle is critical to the dust saltation. Nudging to 6 hourly reanalysis

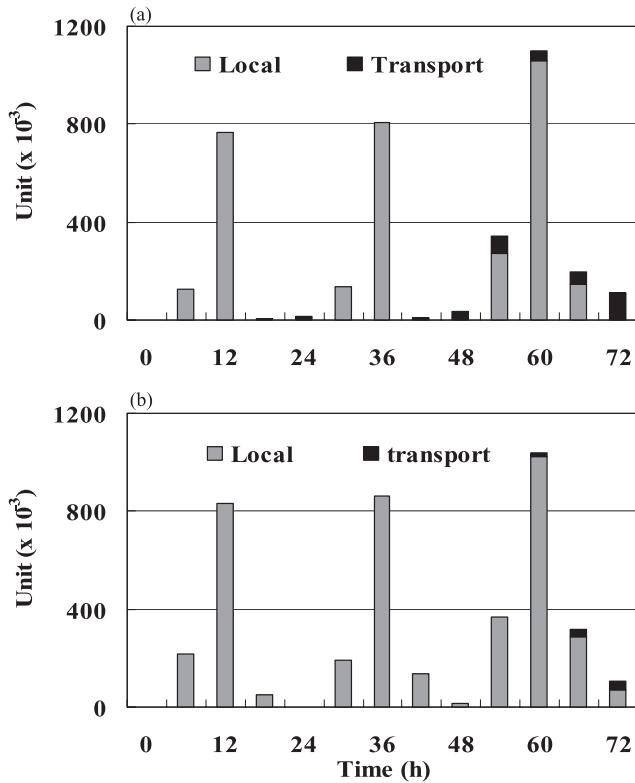


**Figure 11.** Time series of simulated tracer collected at 100-m height in Istanbul. Tracers are contributed from locally emitted (gray color) and transported (black color) for (a) EXP1 and (b) EXP2.

may degrade those smaller scale features. Therefore four dimensional data assimilation was not applied in this case.

[34] The parameters that controlled dust saltation (i.e., the emission rate,  $E_C$ ) were vegetation, soil moisture, and wind speed. In MM5, the US Geophysical Survey (USGS) vegetation data set was chosen and a total of 24 landuse types were categorized. Only the barren type was allowed to generate dust. Within the barren region, 12 soil categories with different ratios of sand, silt, and clay (see Table 1) were taken to be erodible. The name of each soil category and the approximate percentage of the compositions, which were based on Figures 3–16 by *Soil Survey Division Staff* [1993], are listed in Table 1. Note that the soil categories in the MM5T were from a 5-min global United Nations Food and Agriculture Organization (FAO) data set. For non-US applications, Zoebler categories were converted to STATSGO categories. Dust from different soil types was tracked using different tracers, and a total of 12 types (Table 1) were monitored. For wind speed, a minimum threshold value was required for dust uptake. Specifically, based on *Gillette* [1978] and *Tegen and Fung* [1994], an empirical surface dust flux as follows,

$$q_c (\mu\text{g s}^{-1}\text{m}^{-2}) = C(u - u_c)^2,$$

was used, where  $u$  is the 10-m wind speed. The term  $u_c$  is a surface wind speed threshold and a value of  $3 \text{ m s}^{-1}$  was chosen. The dimensional constant,  $C (\mu\text{g s}^2 \text{ m}^{-5})$ , was

simply set to one as suggested by *Tegen and Fung* [1994]. Either the surface friction velocity [*Martcorena and Bergametti*, 1995; *Laurent et al.*, 2005] or 10-m wind speed [*Tegen and Fung*, 1994; *Ginoux et al.*, 2001; *Liu and Westphal*, 2001] has been used for wind saltation. *Colarco et al.* [2003] studied dust emission, transport and deposition for the Puerto Rico Dust Experiment (2000) and compared two different emission models. Their results showed that for central and east African dust sources, the dust emission model from *Ginoux et al.* [2001], which is 10-m wind based, performed better than *Martcorena and Bergametti* [1995], which is a friction velocity based. Therefore a 10-m wind based scheme [i.e., *Gillette*, 1978; *Tegen and Fung*, 1994] was chosen for this study.

[35] The last criterion for dust saltation is the soil water content. Soil must be dry for wind erosion and a critical value of 0.2 of the moist volumetric fraction at the model topsoil layer, which has a depth of 10 cm, was used. Because of the requirement of predicting soil moisture in MM5T, instead of the GDAS reanalysis, the NCEP Global Forecast System (GFS) data, with a spatial resolution of  $1^\circ \times 1^\circ$ , were used in this experiment so that better soil information could be initialized in the MM5T. During the

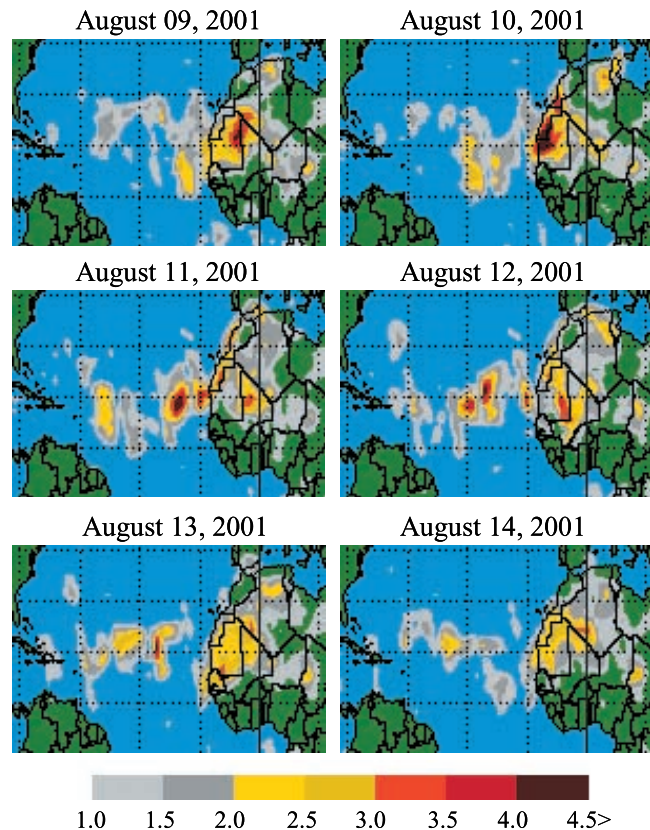


**Figure 12.** The aerosol index for 9, 10, 11, 12, 13, and 14 August from NASA’s Earth Probe/Total Ozone Mapping Spectrometer (EP-TOMS) satellite images (courtesy NASA).

The aerosol index is defined as  $100 \log_{10} \left[ \frac{I_{360}^{meas}}{I_{360}^{Calc}} \right]$ , where  $I_{360}^{meas}$  is the measured 360 nm EP-TOMS radiance and  $I_{360}^{Calc}$  is the calculated 360 nm EP-TOMS radiance for a Rayleigh atmosphere.

**Table 1.** Estimated Percentage of Sand, Silt, and Clay for Each Soil Type Which was Estimated Based on the Figures 3–16 by *Soil Survey Division Staff* [1993]<sup>a</sup>

Soil Types	Percentage, %			Size, $\mu\text{m}$	$V_T$ , cm/s
	Sand	Silt	Clay		
Sand	100	0	0	50	73
Loamy sand	82	10	8	42	58
Sandy loam	62	28	10	33.9	42
Silt loam	20	65	15	16.6	10
Silt	0	100	0	10	4
Loam	40	40	20	24.1	23
Sandy clay loam	60	12	28	31.4	37
Silt clay loam	10	55	35	10.7	5
Clay loam	30	35	35	18.7	12
Sandy clay	50	8	42	26.1	27
Silt clay	8	46	46	8.9	4
Clay	0	0	100	0.7	0.018

<sup>a</sup>The sizes and sedimentation speed ( $V_T$ ) for pure sand, silt, and clay were estimated from *Tegen and Fung* [1994], while the rest were linearly interpolated from these three types according to their compositions.

model integration, the soil moisture could be changed due to precipitation, which in turn would modify the soil flux.

[36] As dusts (tracers) have various sizes, different sedimentation speeds should be used. The sizes and sedimentations of the three basic soil types (i.e., sand, silt, and clay) were based on *Tegen and Fung* [1994], while those of the rest were linearly interpolated from the basic three according to the approximate percentage of their compositions as listed in Table 1.

[37] A shorter time step was required for this case study compared to that of the first case (i.e., 90 s) to prevent numerical instability due to the larger size (or the higher sedimentation speed) of some dust types. For efficiency, various time steps gradually decreasing from 30 to 10 s were used during different integration periods. The MM5T was integrated for 5 d from 1200 UTC 9 August to 1200 UTC 14 August 2001.

## 4.2. Results and Discussions

[38] Figure 13 shows the observed and 60-h simulated soundings at Tamanrasset, Algeria at 0000 UTC (1 a.m. local time) 12 August 2001. Note that northern Africa crosses four different time zones that are 0 to 3 h ahead of the Greenwich Time from west to east. The observed radiosonde indicates that a shallow nocturnal inversion layer near the ground had become established underneath a deep, well-mixed layer (i.e., potential temperature and mixing ratio were almost constant) that extended upward to 530 hPa. Compared with observations, the top of the simulated mixing layer was slightly lower (550 hPa) and the simulated inversion above was weaker and deeper (about 480 to 550 hPa from simulation). In addition, the simulated moisture around 400 hPa was too dry. Wind vectors from observations and model simulations were comparable, except for those above the 250-hPa level. Although there were some discrepancies, simulated results from MM5T were reasonable, in particular for the moisture, temperature, and winds within the mixing and nocturnal inversion layers (i.e., below the level of 550 hPa).

[39] The simulated sea level pressure and 1-km wind vectors after 12-h (0000 UTC), 18-h (0600 UTC), 24-h

(1200 UTC), and 30-h (1800 UCT) integrations are shown in Figure 14. A strong diurnal cycle of low-level winds was presented. Over northern Africa, low-level winds in the night and early morning hours (Figures 14a, 14b, 15a, and 15b) were much stronger than those at midday (Figures 14c and 15c). Winds gradually sped up after the maximum surface heating in the afternoon and became strong again around sunset (Figures 14d and 15d). At night, a strong northerly low-level jet (LLJ) was established (thin and thick black lines in Figures 15a and 15b) and blew from the Mediterranean Sea through Libya and Egypt into the middle and southern Sahara Desert (Figures 14a and 14b). During the day, the surface friction and the coupling of the mixing boundary layer and the surface layer significantly weakened low-level winds (Figures 14c and 15c). However, during the night and early morning the LLJ developed due to the configuration of the strong pressure gradient and the inertial oscillation after the decoupling of the mixing layer from the nocturnal surface layer [*Blackadar*, 1957]. The inertial oscillation is illustrated by the time variation of wind directions (Figure 14), which were almost parallel to the isobars at 0600 UTC (Figure 14b). The level of the maximum wind slightly shifted upward when the nocturnal inversion layer developed deeper, as discussed by *Blackadar* [1957]. The strong pressure gradient resulted from a low close to the Red Sea and a high close to the central Mediterranean Sea. Another southerly to southwesterly nocturnal LLJ occurred at the southeastern border of the Sahara Desert (Figure 14) and had a much smaller coverage area within the desert compared to that of the previous one. The wind was caused by the confluence of the southwesterly monsoon flow and winds induced by a high over the northwestern Indian Ocean, and it was quite strong most of the day and became weaker at the time when the mixed boundary layer was deep (thick gray line in Figure 15c).

[40] Dry erosive soil was mostly located in the Sahara Desert and some countries of the northwestern Middle East within the simulated domain (the thick black contour line in Figure 14b). A diurnal cycle of dust saltation corresponding to the wind pattern was expected, and the primary peak of the averaged surface dust flux occurred in the early morning around 0600 UTC before the mixed boundary layer developed (Figure 16). Therefore due to high winds and high stability within the nocturnal inversion layer, simulated dust amounts at the model's first layer during the nighttime and early morning (Figure 17a) were much higher than those at midday (Figure 17b). It was noticed that two other smaller local maxima of the averaged surface dust flux occurred each day, in particular from the second to the fourth day of the simulation; one broad peak was around 0000 UTC and the other sharper peak was around sunset at 1700 UTC. The causes of these two local maxima will require further investigation.

[41] The mechanism of the dust saltation for this event was different from those previously documented [*Karyampudi*, 1979; *Westphal et al.*, 1988; *Karyampudi et al.*, 1999; *Washington et al.*, 2006]. *Washington et al.* [2006] showed that the dust saltation in Bodele Depression, the largest dust source in the world, was induced by the Bodele Low Level Jet (LLJ). The generation of the Bodele LLJ is enhanced by the topographic channeling between Tibesti and Ennedi mountains in Chad. In a conceptual model for Sahara dust

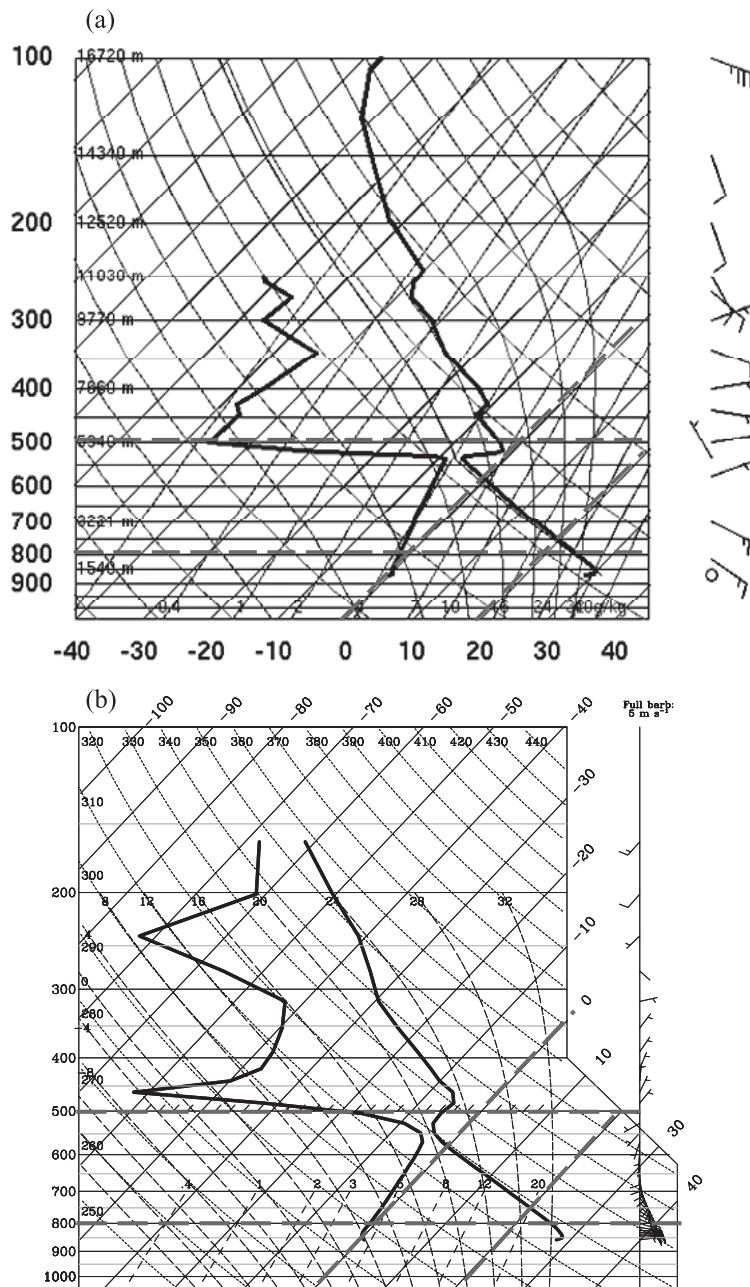


**Figure 13.** (a) Observed (i.e., upper-air sounding) and (b) 60-h simulated skew-T log-P diagrams at Tamanrasset, Algeria at 0000 UTC 12 August 2001. For easy comparison, four gray long-dashed lines were plotted; pressure equal to 500 hPa and 800 hPa, and temperature equal to 0°C and 20°C.

outbreaks [Karyampudi, 1979], the maximum of the dust uptake occurred after strong solar heating and dry convection over the desert (i.e., when the depth of the mixed layer reached its maximum). During the daytime when the mixed boundary layer deepened and reached the maximum, the momentum transported downward from the Middle Level Easterly Jet (MLEJ) at 600–700 hPa. This resulted in strong surface winds that mobilized dust.

[42] Another mechanism for dust saltation was proposed by Westphal *et al.* [1988] using model simulations with a resolution of 220 km. They revealed that during the dust outbreaks on 25–26 August 1974 the maximum dust uptake

occurred at the north of the MLEJ before the depth of the boundary layer reached its maximum. In this scenario, LLJs that were associated with a shallow easterly wave where the momentum was transported downward after the mixing in the boundary layer caused peak dust uptake. The same mechanism was also applied to the dust outbreak during 10–19 September 1994 studied by Karyampudi *et al.* [1999] using reanalysis and observations. In the dust event studied here, although the primary mechanism of the dust saltation also resulted from LLJs, those jets occurred during the night and early morning (i.e., nocturnal LLJs) and were induced by strong pressure gradients and the inertial oscil-

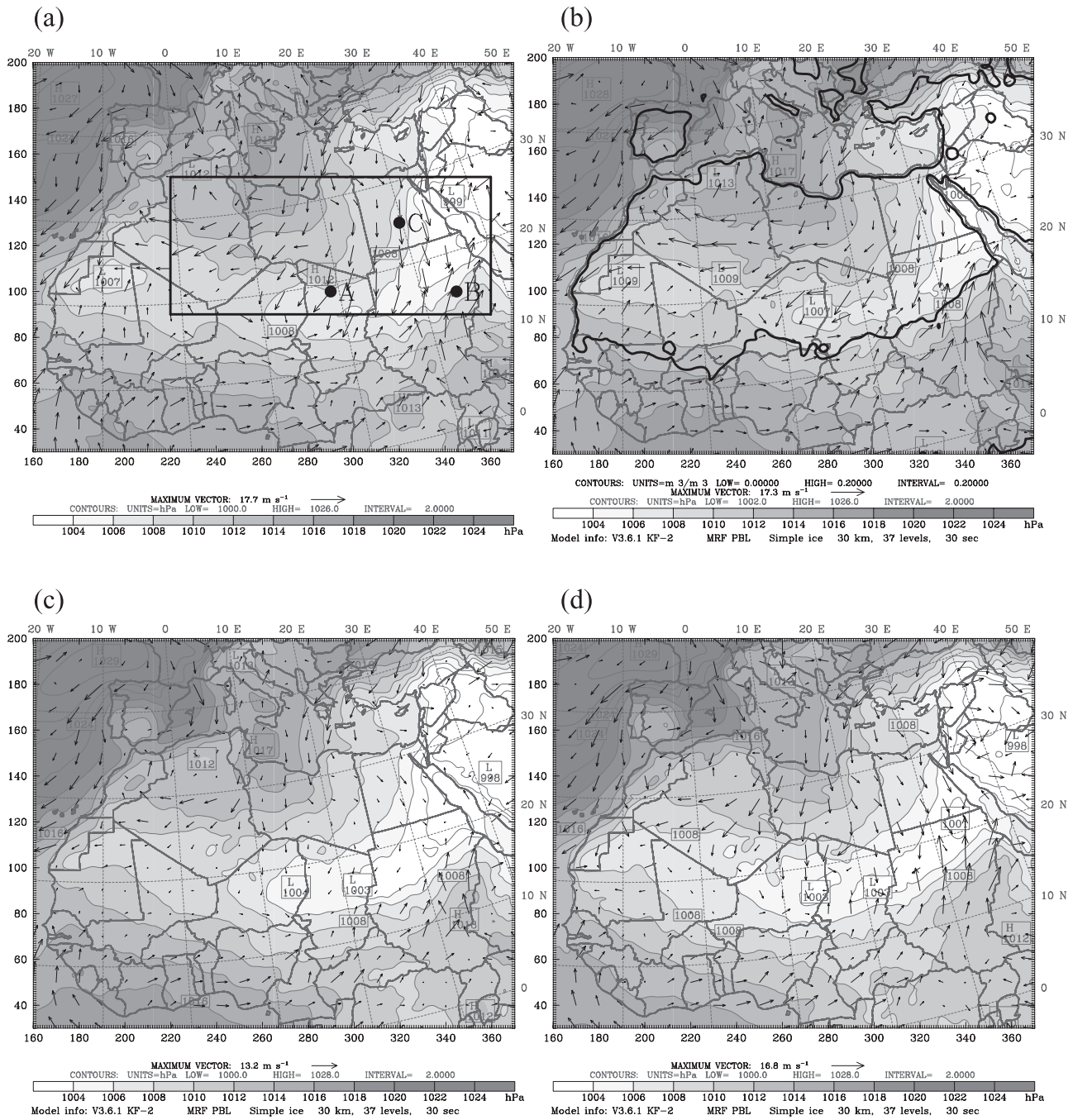


**Figure 14.** Simulated sea level pressure (shaded and gray contours) and 1-km wind vectors after (a) 12-h (0000 UTC), (b) 18-h (0600 UTC), (c) 24-h (1200 UTC), and (d) 30-h (1800 UTC) integrations. In Figure 14a, points A to C are locations for the plots in Figure 15 and the rectangular box is the area for the calculation of the average surface dust flux in Figure 16. The thick black contour line in Figure 14b indicates the simulated moist volumetric fraction that equals to 0.2 after an 18-h integration.

lation. The maximum dust saltation took place in the early morning, right before the mixed boundary layer developed. Moreover, simulated dust was uplifted into the atmosphere primarily in the northern and northeastern Saharan Desert, which were away from the MLEJ.

[43] Figure 18 shows the simulated 1.5-km temperature, 4-km winds, 100-m and 3-km dust mixing ratio, and column integrated dust. A warm air mass developed above the Sahara Desert due to high surface sensible heat flux and

propagated westward into the eastern Atlantic Ocean. Over the desert, due to the thermal wind balance, the MLEJ at the 4-km height ( $\sim 630$  hPa) was located at the southern edge of the warm Saharan air below (Figure 18a). From late 10 to early 11 August, a simulated dust plume was transported into the Atlantic Ocean through Western Sahara and Mauritania (Figure 18b) as observed from the TOMS satellite aerosol index (Figure 12). The primary types of the dust that were injected into the atmosphere over the desert and northwest-

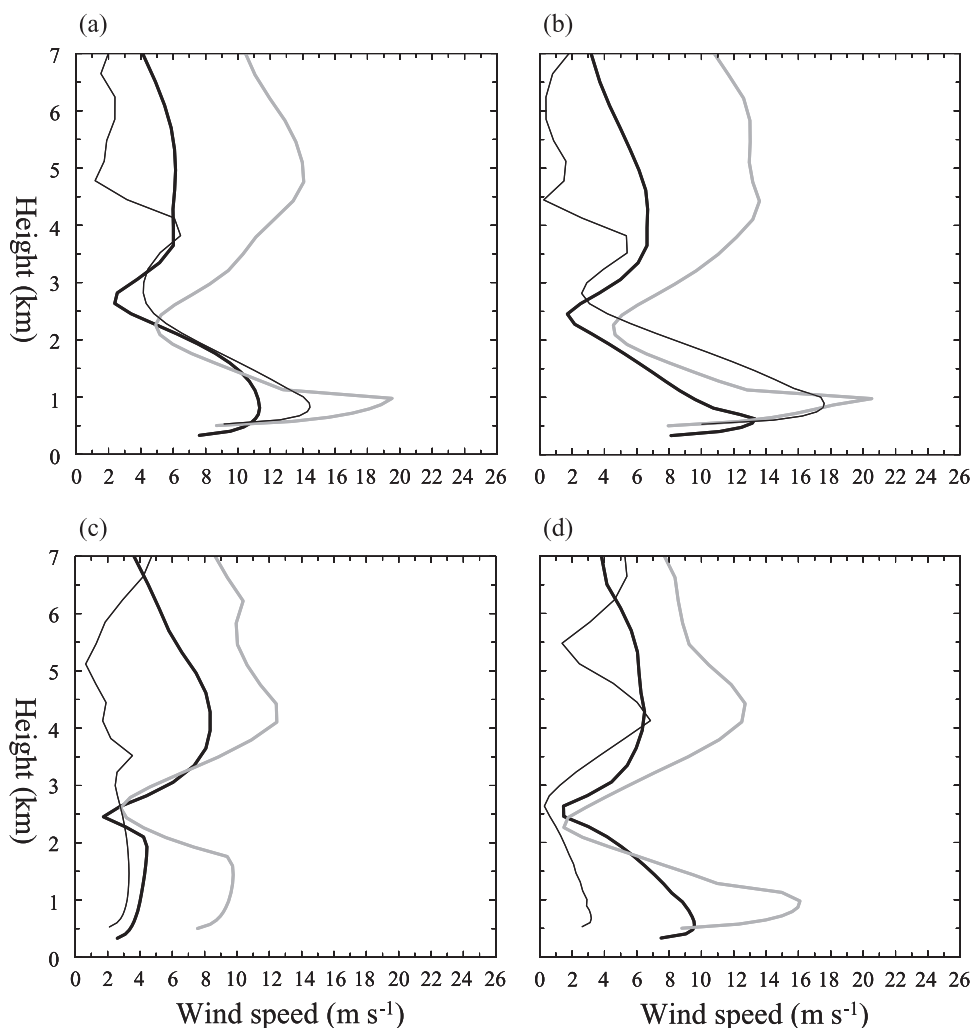


**Figure 15.** Vertical profile of wind speed after (a) 12-h (0000 UTC), (b) 15-h (0300 UTC), (c) 24-h (1200 UTC), and (d) 30-h (1800 UTC) integrations. The thin black, thick gray, and thick black lines indicate the points A, B, and C from Figure 14a, respectively.

ern countries in Middle East were loam and clay (Figure 19), which have average radii of approximately 24 and  $0.7 \mu\text{m}$ , respectively. Note that the soil type over most of the Sahara Desert is loam. Only limited small, scattered regions are covered by clay, such as the northwest corner of West Sahara, the northeast corner of Algeria, and the northwest corner of Middle East. When there was no wet process (i.e., no clouds), fine clay particles could be suspended in the air long enough to accumulate to a significant amount after a couple of days (Figures 19c and 19d).

[44] At the southern edge of the MLEJ, a simulated easterly wave disturbance was located on the lee side of the coastal mountains. The wave disturbance propagated into the Atlantic Ocean and became a closed low-pressure system. After a 27-h integration (Figure 18b), the system reached a pressure of 729 hPa at 2.8 km and a sea level pressure (SLP) of 1011 hPa. Off the coast, the simulated easterly jet curved northward cyclonically toward the dust plume and the SAL, as shown in Figures 18a and 18b. At the northern edge of the MLEJ, a simulated closed anticyclonic eddy, which was located off the African coast and the

northeast of the low-pressure system, was first formed at approximately 2.8 km with a strength of 737.2 hPa after a 27-h simulation (Figure 18b). A similar anticyclonic eddy off the African coast was also presented in other studies [Carlson and Prospero, 1972; Karyampudi and Carlson, 1988; Karyampudi *et al.*, 1999; Karyampudi and Pierce, 2002]. Karyampudi and Carlson [1988] commented that in their simulations, a resolution of at least 110 km was required in order to resolve this eddy and a higher resolution of 30 km is used here.

[45] The low-pressure system (i.e., the storm Chantal) propagated northwestward, and the MLEJ at the north side of the system merged into the elevated SAL and the dust plume after a 36-h simulation (figure not shown). Therefore simulated dust and warm dry air started interacting with Chantal from the north side of the storm at that time. The simulated storm weakened from 0000 UTC to 0600 UTC 11 August 2001 (i.e., 42-h to 48-h simulations; figure not shown) and this weakening scenario was also reported by the National Hurricane Center. After a 60-h simulation, at 0000 UTC 12 August (Figure 18d), the anticyclonic eddy at

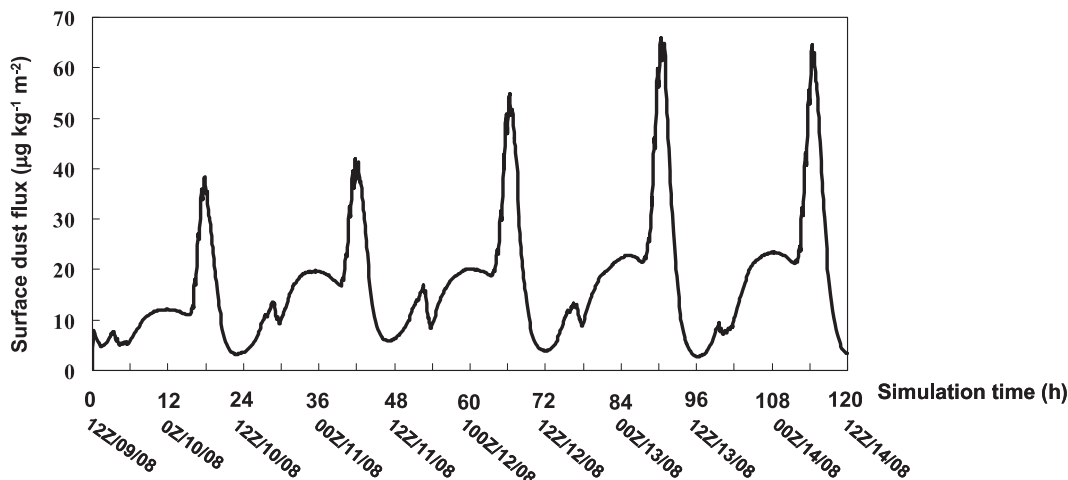


**Figure 16.** Time series of the average surface dust flux ( $\mu\text{g kg}^{-1} \text{m}^{-2}$ ) from the rectangular area in Figure 14a.

2.8 km was enhanced to 738 hPa, and the storm deepened to a pressure of 726.1 hPa at 2.8 km and a SLP of 1007 hPa. The depths of the SAL at the locations of points A and B in Figure 18c were from a base of about 880 and 850 hPa to a top of about 580 and 550 hPa, respectively (Figure 20a). The trade wind inversion below the SAL was clearly simulated and the mixed boundary layer over the ocean became slightly deeper when it moved toward the west (i.e., the height of the SAL base or the trade wind top increased when it propagated westward). Compared with simulation result, the SAL and the trade wind inversion from the NCEP GFS reanalysis (Figure 20b) were weaker. Saharan dust and warm air intruded into the storm center after a 66-h simulation (figures not shown), at the time when the storm and the anticyclonic eddy began to weaken slowly. After a 120-h simulation, the storm and the anticyclonic eddy had a pressure of 729.7 hPa and 733.9 hPa, respectively, at 2.8 km (Figure 18f). Saharan dust was also transported into the anticyclonic eddy region (Figure 18f) as proposed in the Saharan dust concept model [Karyampudi, 1979; Karyampudi *et al.*, 1999].

[46] Compared with GFS reanalysis, the simulated temperature, MLEJ, and large scale patterns after a 60-h integration were quite reasonable over both land and ocean (Figures 18c versus 21a and Figures 18d versus 21b). In the reanalysis, Chantal and the anticyclonic eddy were weakly presented in the wind vector field and the middle level jet north of Chantal was not as strong as simulation results (Figure 21a). These could be because the resolution from the reanalysis was too coarse ( $1^\circ \times 1^\circ$ ). After 120-h (i.e., 5 d) integration (Figures 18e versus 21c and Figures 18f versus 21d), the simulated MLEJ over land was oriented in an east-west direction, while the reanalysis showed an east-southeast to west-northwest direction. The difference between reanalysis and model simulation over the ocean was even more significant. The simulated high wind close to the western boundary of the plotted domain moved too far southward and the simulated warm air intruded into Atlantic Ocean more than that of reanalysis. Simulated Chantal was

slightly stronger (1010 hPa versus 1014 hPa for the sea level pressure) and was drifted northward, while the storm position from reanalysis was close to the observed. Note that the observed Chantal's positions, which are marked in Figure 18f, are 6 h (i.e., black bullet) and 12 h (gray bullet) after the plotted time (i.e., 1200 UTC 14 August 2001) since no data was available before then. The anticyclonic eddy, which usually follows behind the westerly wave disturbance, was still not well resolved.

[47] The transport of the Saharan dust (Figures 18b, 18d, and 18f) was qualitatively, if not quantitatively, consistent with that from TOMS satellite images in Figure 12. The simulated dust amount in the atmosphere might be underestimated, in particular over the ocean, because there was no dust in the model initial conditions (i.e., dust that would be uplifted into the atmosphere before the model initial time was excluded). Because of subsidence, dust could exist below the elevated SAL over the ocean (green contours in Figures 18a, 18c, 18e, and 22). Different types of dust had different subsiding speeds during transport (Table 1). In this study, most large dust particles reached the ground before they made it to the Atlantic (Figures 19a, 19b, 19e, and 19f), and clay was the primary soil type that was transported to the ocean (Figures 19c and 19d). Note that if the upward motion were strong over the desert (e.g., using a higher model resolution), uplifting dust to higher levels, or if the MLEJ were stronger, larger dust particles might be transported to the Atlantic. As some clay subsided into the cool and clean northeasterly trade wind zone, it was advected southwestward. Therefore simulated dust within the trade wind boundary layer (green contours in Figures 18a, 18c and 18e) was shifted southward compared to that within the SAL (white contours in Figures 18a, 18c, and 18e). This is consistent with observations reported by Karyampudi *et al.* [1999, Figure 22a]. Although the simulated dust that interacted with the storm over the ocean was mainly from the northwestern region of the Western Sahara (i.e., clay; Figures 18b, 18d, and 18f), it is possible that dust from other regions, in particular for those clay dust areas, had an

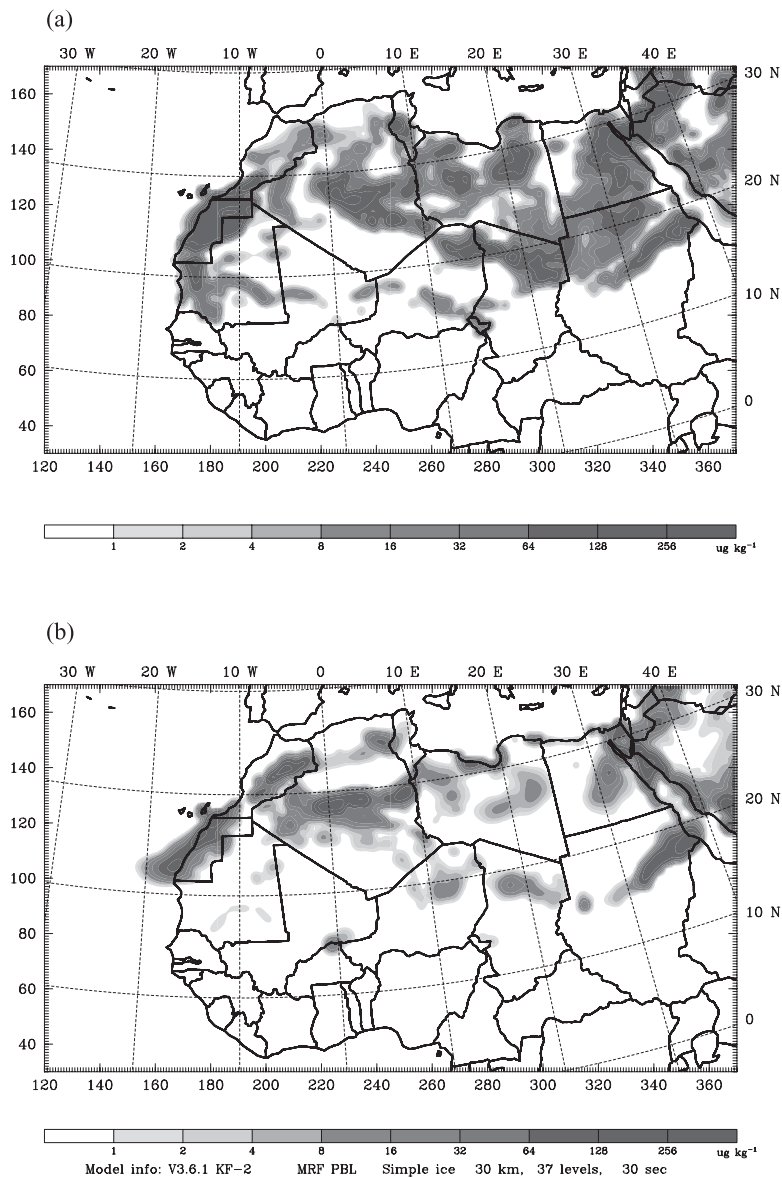


**Figure 17.** Simulated mixing ratio of the total dust ( $\mu\text{g kg}^{-1}$ ) at the model's first layer close to the surface after (a) 12-h and (b) 24-h integrations.

interaction with Chantal if the dust present at the model initial time was included.

[48] *Dunion and Velden* [2004] showed that the storm Chantal was never able to separate from the SAL and struggled to maintain its intensity. Although only data after 0000 UTC 15 August were used in their study, it is very

likely that the influence of Saharan air and dust on Chantal was earlier than 0000 UTC 15 August, as is shown here.

## 5. Concluding Remarks

[49] An online tracer model based on the fifth-generation Penn State/NCAR Mesoscale model, called MM5T, was

**Figure 18.** Simulated 1.5-km temperature (K; color shaded), 4-km wind speed (red contours), and mixing ratio of the total dust ( $\mu\text{g kg}^{-1}$ ) at 100 m (green contours) and 3 km (white contours) with a multiplicative contour interval of 10 after (a) 27-h (1500 UTC 10 August), (c) 60-h (0000 UTC 12 August), and (e) 120-h (1200 UTC 14 August) simulations. Wind speed stronger than  $12 \text{ ms}^{-1}$  was plotted. Figures 18b, 18d, and 18f were the same simulated times as Figures 18a, 18c, and 18e, respectively, except for column integrated dust ( $\times 10^3 \mu\text{g m}^{-2}$ ; gray shaded) with a multiplicative contour interval of 1.5, 4-km wind vectors, 2.8-km pressure (blue lines), and sea level pressure (orange lines). Black and gray dots in Figure 18e are the Chantal positions at 1800 UTC 14 August and 0000 UTC 15 August, respectively, and the information was obtained from <http://www.wunderground.com/hurricane/at20013.asp>. Points A and B in Figure 18c are locations for sounding plot in Figure 20.



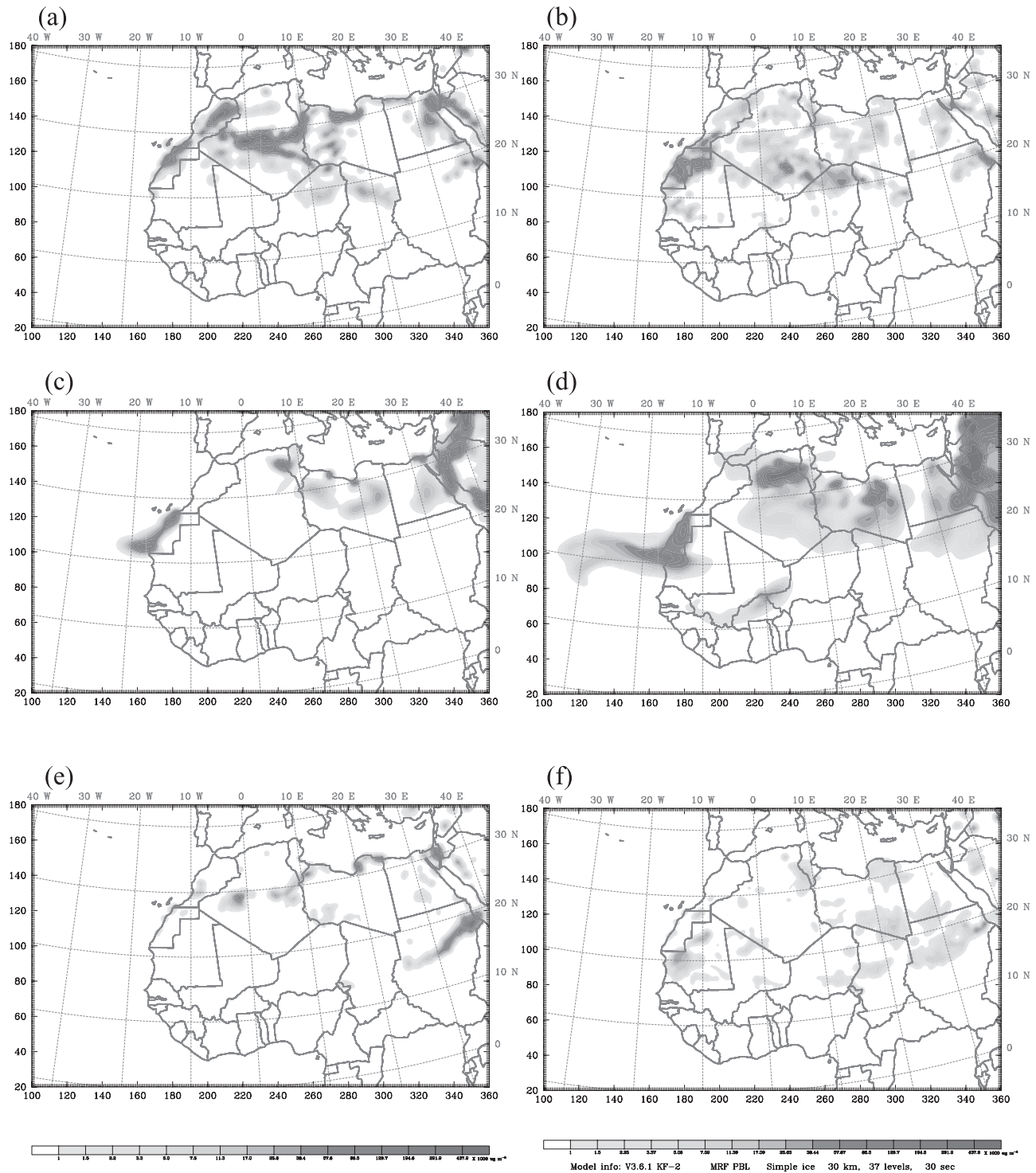


**Figure 19.** Column integrated (a) loam, (c) clay, and (e) all 10 other dust types ( $\times 10^3 \mu\text{g m}^{-2}$ ) with a multiplicative contour interval of 1.5 after a 27-h simulation. Figures 19b, 19d, and 19f are the same information as in Figures 19a, 19c, and 19e, respectively, except for a 60-h simulation.

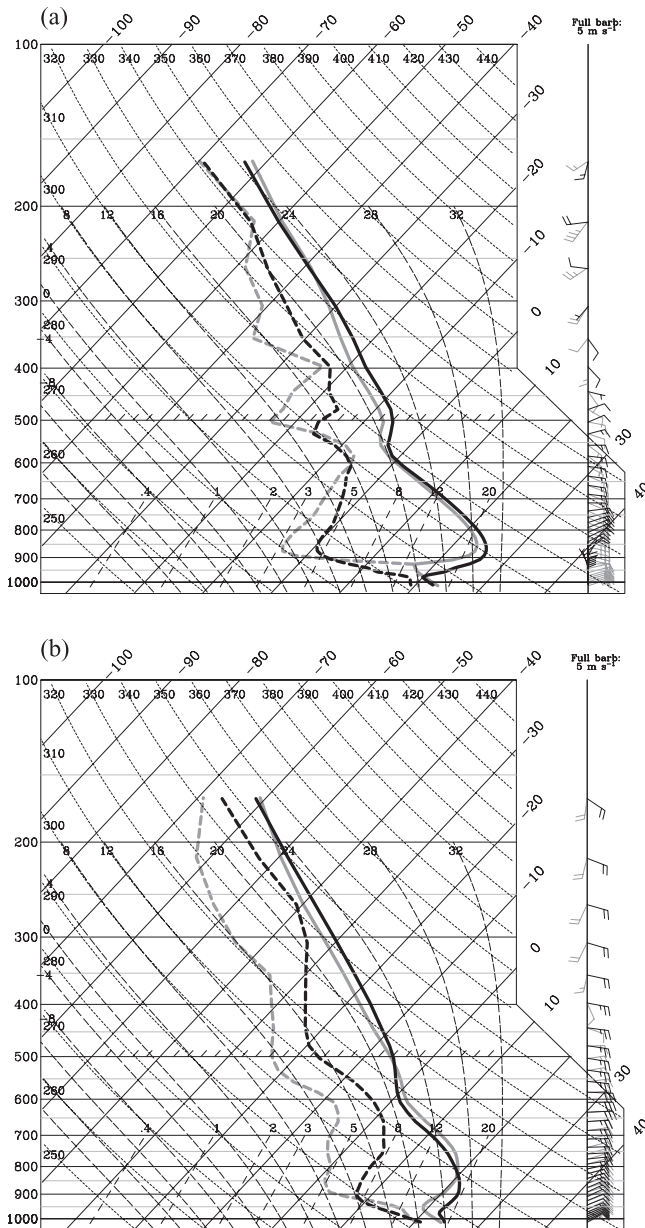


**Figure 20.** Skew T-log P diagram at 0000 UTC 12 August 2001 at points A (black lines) and B (gray lines) in Figure 18c from (a) the 60-h model simulation and (b) NCEP GFS reanalysis.

developed to identify the sources or types of long-range pollutant transport more accurately and precisely than comparable off-line models. The effects on tracer transport due to advection, boundary layer mixing, cumulus convective mixing, and sedimentation were taken into account. Two high-pollution events in Istanbul, Turkey on 7–8 and 10–12 January 2002 and one Saharan dust transport on 10–14 August 2001 were studied using the MM5T.

[50] For the study of pollution episodes in Istanbul, four dimensional data assimilation (i.e., nudging to reanalysis) was applied to keep the large scale features better during simulations. Different tracers were used to represent pollutants released from selected cities on different days, using a

diurnal cycle of emission rate that was maximized at 5 p.m. local time. In this semi-idealized study, the same emission rate was applied to all selected cities. The first step in analyzing the model results was to verify accurate simulation of meteorological fields, especially the low-level wind fields that play a crucial role in transport calculations. Time series of low-level wind and temperature fields in the vicinity of Istanbul showed good agreement with local observations, except the strong diurnal surface temperature oscillation at Uzunkopru. The inaccuracy of the simulated surface temperature was due to the nudging of reanalysis which could harm the shorter time-scale features, such as the diurnal cycle. The model also failed to reasonably catch the weak wind condition, which is a common problem for most numerical models. MM5T reproduced the larger-scale patterns well after nudging to reanalysis and this is important for long-range transport. In particular, it simulated a surface high-pressure system over central Europe and a surface low over western Russia, with a substantial pressure gradient between these two systems. This gradient induced strong north-northwesterly low-level flow capable of transporting upstream pollutants toward Istanbul. Moreover, the model reproduced a strong frontal inversion in the early time period and a subsequent subsidence inversion over the path of tracer transport. The inversion suppressed the development of the planetary boundary layer and effectively trapped low-level pollutants near the ground. These weather conditions created a favorable environment for long-range transport and limited dilution of pollutants.

[51] Results showed that pollutants originating in Bucharest, Silesia and Krakow, and Warsaw (only Bucharest in Romania and Silesia and Krakow in Poland for the second event) could have contributed to two high-pollution episodes on 7–8 and 10–12 January 2002 in Istanbul. Pollutants originating in Bucharest could have arrived in Istanbul after 24 h, while those emitted in Silesia and Krakow would have appeared after 36 h. Given the meteorological conditions associated with these events, and an assumption that emission rates were identical in all cities, MM5T indicated that pollutants from Bucharest would have made the largest contribution to remotely generated pollution during these events, with those from Silesia and Krakow not far behind. While MM5T indicated that remote sources of pollution made relatively small contributions to the total pollutant concentration in Istanbul during most peak local emission times, a contribution of 3.3% from long-range transport could occur at the times of highest local contribution. Remote sources could account for up to 20 ~ 25% at the times off the peak when pollution was still relatively high in Istanbul. Although there are some uncertainties in the MM5T calculation, the value of 3.3% is conservative since only limited cities were examined in this demonstration. In contrast, imported pollutants could have become predominant when local emissions were near minimum values. It is believed that MM5T performed reasonably. However, one should also keep in mind that some uncertainties can be associated with simulated results due to the assumptions made in the model.

[52] For the study of Saharan dust transport, the nudging to reanalysis was deactivated since the smaller scale features of the diurnal cycle are important to dust saltation. During simulations, twelve types of dust from northern Africa and

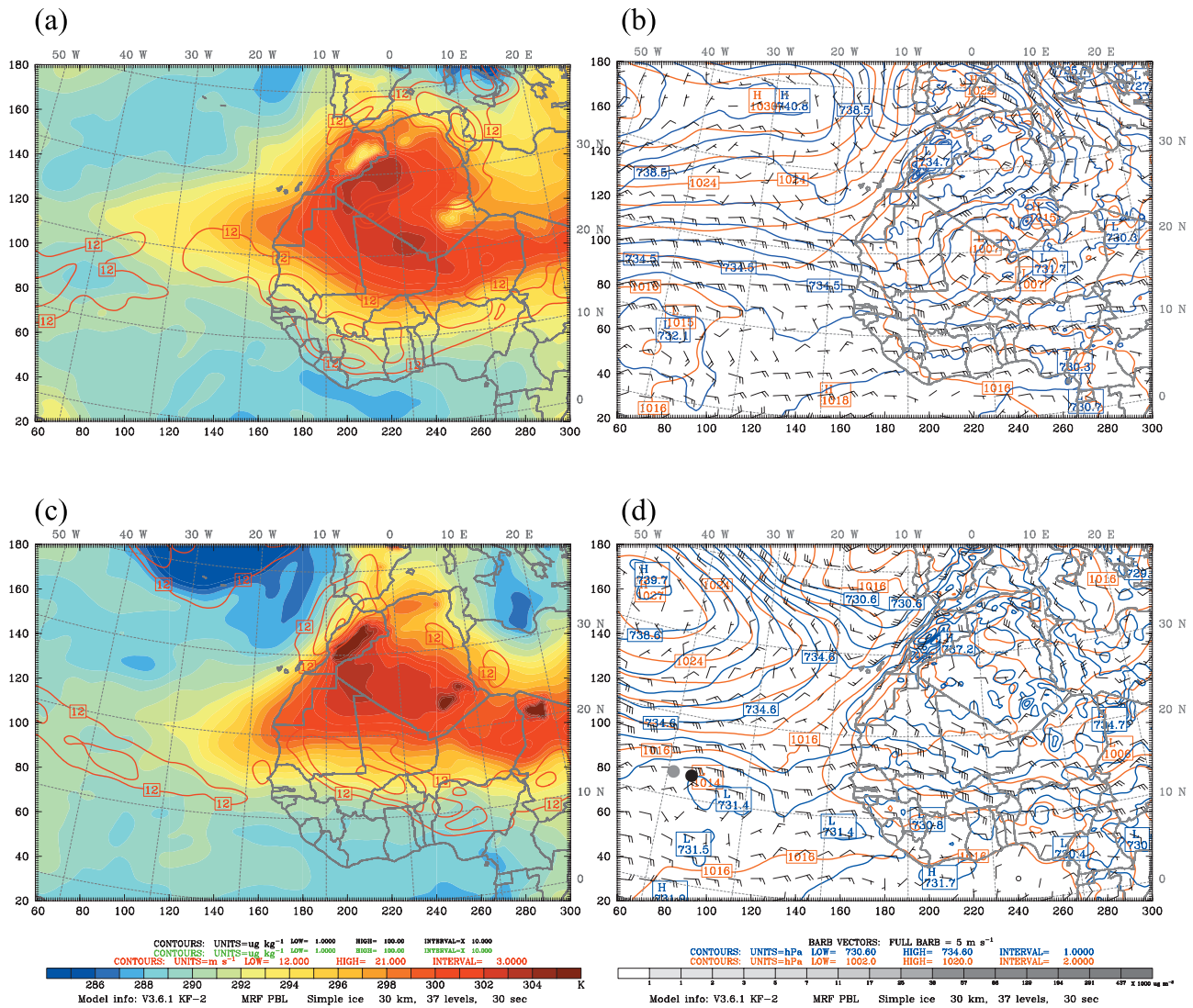


**Figure 21.** The 1.5-km temperature (K; color shaded) and 4-km wind speed (red contours) at (a) 0000 UTC 12 August and (c) 1200 UTC 14 August from GFS reanalysis. Wind speed stronger than  $12 \text{ ms}^{-1}$  was plotted. Figures 21b and 21d were the same reanalysis times as Figures 21a and 21c, respectively, except for 4-km wind vectors, 2.8-km pressure (blue lines), and sea level pressure (orange lines). Black and gray dots in Figure 21d were the Chantal positions at 1800 UTC 14 August and 0000 UTC 15 August, respectively.

northwestern countries in the Middle East were tracked separately. Thus the dust types that potentially interacted with Tropical Storm Chantal (2001) could be identified. Compared with observations (i.e., radiosonde and satellite images) and reanalysis, simulated meteorological conditions and dust transport from MM5T were reasonable, in particular before 60-h simulation. The characteristics of the Saharan Air Layer (SAL), the Middle Level Easterly Jet (MLEJ), the easterly wave disturbance which became the storm Chantal, and the anticyclonic eddy to the north of the MLEJ off the African coast were reasonably reproduced by the MM5T. However, the simulated Chantal moved too far to the north after a 5-d integration. Because of the thermal wind balance, MLEJ at 600–700 hPa was located at the southern edge of the warm, dry Saharan air below. The anticyclonic eddy first

formed around 2.8-km height off the African coast after a 28-h simulation.

[53] Vegetation type, soil moisture, and wind speed were parameters used to control dust saltation. Different types of soil were assigned with different sedimentation speeds according to their compositions. The maximum amount of the surface dust flux occurred in the early morning right before sunrise and was mostly located in the northern and northeastern Sahara Desert, away from the MLEJ. It was found that the primary mechanism of the dust saltation for the event studied here was a nocturnal low-level jet (LLJ), and it was different from those previously documented (i.e., MLEJ and LLJs that were associated with a shallow easterly wave). The nocturnal LLJ developed due to the configuration of the strong pressure gradient and the inertial oscillation after the decoupling of the mixing layer from the

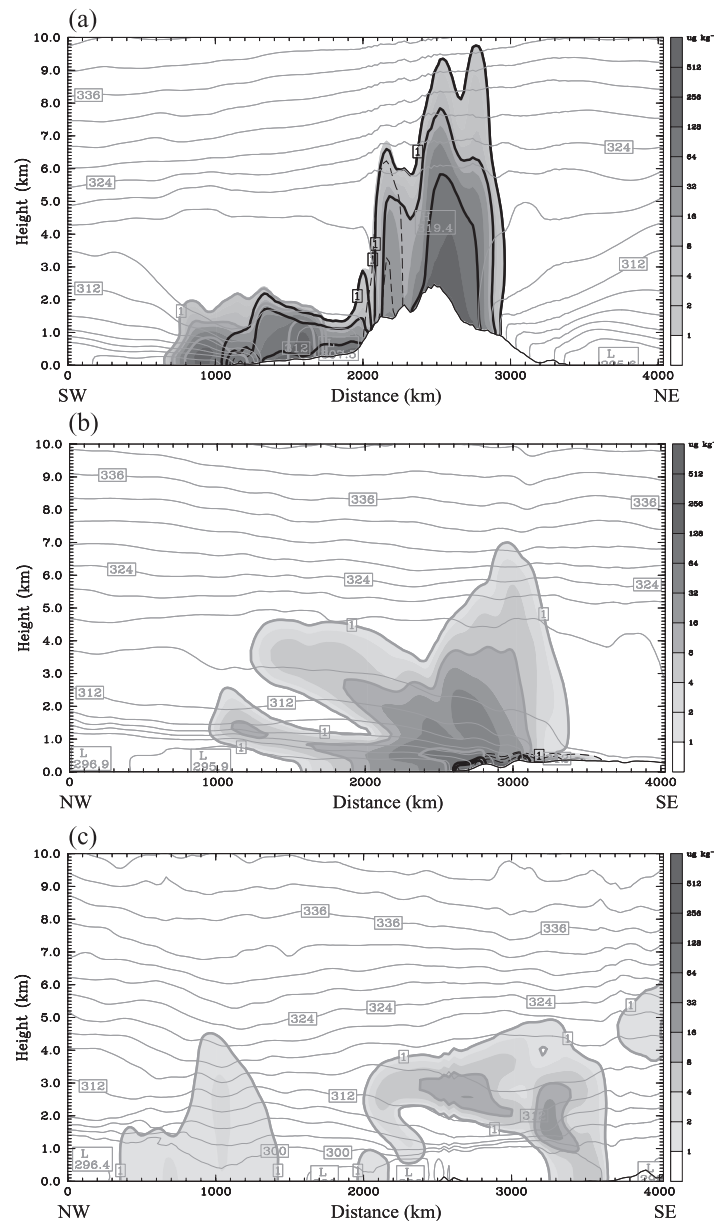


**Figure 22.** Vertical cross sections of simulated potential temperature (K; thin gray contours) and the total dust mixing ratio ( $\mu\text{g kg}^{-1}$ ; shaded) after (a) 27-h, (b) 60-h, and (c) 120-h simulations with a multiplicative contour interval of 2. The thick gray lines, thick black lines, and thin-dashed black lines are the mixing ratios for clay, loam, and the sum of the remaining 10 soil types, respectively, with a multiplicative contour interval of 8. The vertical cross sections of Figures 22a, 22b, and 22c correspond to the black lines in Figures 18a, 18c, and 18e, respectively.

nocturnal inversion layer below [Blackadar, 1957]. It is interesting to see that the soil type over the Sahara Desert was mostly loam; nevertheless, for the event studied here the dust type that was propagated to the Atlantic Ocean was clay because of its small size, while the other types were sedimented to the ground before reaching the ocean. Because of the northeasterly trade wind, dust that fell into the lower boundary layer was advected southwestward, spatially shifted from that in the SAL above. Note that the simulated dust, in particular for those small particulates, was very likely underestimated because dust in the initial field was ignored.

[54] Simulation results showed strong evidence that Chantal interacted with Saharan dust, primarily the type of clay from the northwestern corner of West Sahara, after propagating into the eastern Atlantic Ocean at a very early stage of the storm development. The Saharan dust and warm air started interacting with Chantal from the north side of the storm after a 36-h simulation (0000 UTC 11 August, 2001) and by a 66-h simulation the dust and warm air were advected into the center of the storm. Dust also propagated toward the anticyclonic eddy as documented in other studies. The impact of Saharan dust on storm genesis and development is very important and interesting. We will

continue our efforts in this direction in the future. To accomplish this, the interaction between the dust and radiation and between the dust and cloud microphysics, which has an indirect impact on radiation budget, will be implemented into the MM5T.

[55] **Acknowledgments.** The authors would like to thank Jih-Ying Chen and Kemal Gurer who helped generate Figure 4. Thanks are extended to Thomas Gill at University of Texas, El Paso for providing soil information for our model calculation. TOMS aerosol images used in this study were acquired as part of NASA's Earth-Sun System Division and archived and distributed by the Goddard Earth Sciences (GES) Data and Information Services Center (DISC) Distributed Active Archive Center (DAAC). This study was mainly supported by the NASA-NAG5-13678 project. Additional support was provided by the University of California Toxic Substances Research and Teaching Program (TSR&TP) through the Atmospheric Aerosols and Health Lead Campus Program.

## References

- Bergametti, G., L. Gomes, G. Coudegaussen, P. Rognon, and M. N. Lecoustumer (1989), African dust observed over Canary Islands - Source-regions identification and transport pattern for some summer situations, *J. Geophys. Res.*, *94*, 14,855–14,864.
- Blackadar, A. K. (1957), Boundary layer wind maxima and their significance for the growth of nocturnal inversions, *Bull. Am. Meteorol. Soc.*, *38*, 283–290.
- Carlson, T. N., and J. M. Prospero (1972), The large-scale movement of Saharan air outbreaks over the northern equatorial Atlantic, *J. Appl. Meteorol.*, *11*, 283–297.
- Chin, M., P. Ginoux, S. Kinne, O. Torres, B. N. Holben, B. N. Duncan, R. V. Martin, J. A. Logan, A. Higurashi, and T. Nakajima (2002), Tropospheric aerosol optical thickness from the GOCART model and comparisons with satellite and sun photometer measurements, *J. Atmos. Sci.*, *59*, 461–483.
- Chin, M., P. Ginoux, R. Lucchesi, B. Huebert, R. Weber, T. Anderson, S. Masonis, B. Blomquist, A. Bandy, and D. Thornton (2003), A global aerosol model forecast for the ACE-Asia field experiment, *J. Geophys. Res.*, *108*(D23), 8654, doi:10.1029/2003JD003642.
- Colarco, P. R., O. B. Toon, and B. N. Holben (2003), Saharan dust transport to the Caribbean during PRIDE: 1. Influence of dust sources and removal mechanisms on the timing and magnitude of downwind aerosol optical depth events from simulations of in situ and remote sensing observations, *J. Geophys. Res.*, *108*(D19), 8589, doi:10.1029/2002JD002658.
- Dudhia, J. (1989), Numerical study of convection observed during the winter monsoon experiment using a mesoscale two-dimensional model, *J. Atmos. Sci.*, *46*, 3077–3107.
- Dunion, J. P., and C. S. Velden (2004), The impact of the Saharan air layer on Atlantic tropical cyclone activity, *Bull. Am. Meteorol. Soc.*, *85*, 353–365.
- Gillette, D. (1978), A wind tunnel simulation of the erosion of soil: Effect of soil texture, sandblasting, wind speed, and soil consolidation on dust production, *Atmos. Environ.*, *12*, 1735–1743.
- Ginoux, P., M. Chin, I. Tegen, J. M. Prospero, B. Holben, O. Dubovik, and S. Lin (2001), Sources and distributions of dust aerosols simulated with the GOCART model, *J. Geophys. Res.*, *106*, 20,255–20,274.
- Grell, G. A., J. Dudhia, and D. R. Stauffer (1995), A description of the fifth-generation Penn State/NCAR mesoscale model (MM5), *NCAR/TN-398 + STR*, 122 pp., National Center for Atmospheric Research, Boulder, Colo.
- Hogrefe, C., J. Biswas, B. Lynn, K. Civerolo, J.-Y. Ku, J. Rosenthal, C. Rosenzweig, R. Goldberg, and P. L. Kinney (2004), Simulating regional-scale ozone climatology over the eastern United States: Model evaluation results, *Atmos. Environ.*, *38*, 2627–2638.
- Hong, S.-Y., and H.-L. Pan (1996), Nonlocal boundary layer vertical diffusion in a medium-range forecast model, *Mon. Weather Rev.*, *124*, 2322–2339.
- Jimenez, P., R. Parra, S. Gasso, and J. M. Baldasano (2005), Modeling the ozone weekend effect in very complex terrains: A case study in the northeastern Iberian Peninsula, *Atmos. Environ.*, *39*, 429–444.
- Kain, J. S. (2004), The Kain-Fritsch convective parameterization: An update, *J. Appl. Meteorol.*, *43*, 170–181.
- Kallos, G., et al. (1997), The regional weather forecasting system SKIRON: An overview, in *Proceedings of the Symposium Regional Weather Prediction on Parallel Computer Environments*, edited by G. Kallos, V. Kotroni, and K. Lagouvardos, pp. 109–122, Univ. of Athens, Greece.
- Kallos, G., V. Kotroni, K. Lagouvardos, and A. Papadopoulos (1998), On the long-range transport of air pollutants from Europe to Africa, *Geophys. Res. Lett.*, *25*, 619–622.
- Kallos, G., A. Papadopoulos, P. Katsafados, and S. Nickovic (2006), Transatlantic Saharan dust transport: 1. Model simulation and results, *J. Geophys. Res.*, *111*, D09204 doi:10.1029/2005JD006207.
- Karyampudi, V. M. (1979), A detailed synoptic-scale study of the structure, dynamics, and radiative effects of the Saharan air layer over the eastern tropical Atlantic during GARP Atlantic Tropical Experiment, Master's thesis, Department of Meteorology, The Pennsylvania State University, 135 pp.
- Karyampudi, V. M., and T. N. Carlson (1988), Analysis and numerical simulations of the Saharan air layer and its effect on easterly wave disturbances, *J. Atmos. Sci.*, *45*, 3102–3136.
- Karyampudi, V. M., and H. F. Pierce (2002), Synoptic-scale influence of the Saharan air layer on tropical cyclogenesis over the eastern Atlantic, *Mon. Weather Rev.*, *130*, 3100–3128.
- Karyampudi, V. M., et al. (1999), Validation of the Saharan dust plume conceptual model using Lidar, Meteosat, and ECMWF data, *Bull. Am. Meteorol. Soc.*, *80*, 1045–1075.
- Kindap, T., A. Unal, S.-H. Chen, Y. Hu, M. T. Odman, and M. Karaca (2006), Long-range aerosol transport from Europe to Istanbul, Turkey, *Atmos. Environ.*, *40*, 3536–3547.
- Kinne, S., et al. (2003), Monthly averages of aerosol properties: A global comparison among models, satellite data, and AERONET ground data, *J. Geophys. Res.*, *108*(D20), 4634, doi:10.1029/2001JD001253.
- Kishcha, P., et al. (2007), Forecast errors in dust vertical distributions over Rome (Italy): 1. Multiple particle size representation and cloud contributions, *J. Geophys. Res.*, *112*, D15205, doi:10.1029/2006JD007427.
- Kubilyay, N., S. Nickovic, C. Moulin, and F. Dulac (2000), An illustration of the transport and deposition of mineral dust onto the eastern Mediterranean, *Atmos. Environ.*, *34*, 1293–1303.
- Laurent, B., B. Marticorena, G. Bergametti, P. Chazette, F. Maignan, and C. Schmechtig (2005), Simulation of the mineral dust emission frequencies from desert areas of China and Mongolia using an aerodynamic roughness length map derived from the POLDER/ADEOS 1 surface products, *J. Geophys. Res.*, *110*, D18504, doi:10.1029/2004JD005013.
- Lee, S.-M., S.-C. Yoon, and D. W. Byun (2004), The effect of mass inconsistency of the meteorological field generated by a common meteorological model on air quality modeling, *Atmos. Environ.*, *38*, 2917–2926.
- Liu, M., and D. L. Westphal (2001), A study of the sensitivity of simulated mineral dust production to model resolution, *J. Geophys. Res.*, *106*, 18,099–18,112.
- Liu, M., D. L. Westphal, S. Wang, A. Shimizu, N. Sugimoto, J. Zhou, and Y. Chen (2003), A high-resolution numerical study of the Asian dust storms of April 2001, *J. Geophys. Res.*, *108*(D23), 8653, doi:10.1029/2002JD003178.
- Liu, M., D. L. Westphal, A. L. Walker, T. R. Holt, K. A. Richardson, and S. D. Miller (2007), COAMPS real-time dust storm forecasting during Operation Iraqi freedom, *Weather Forecasting*, *22*, 192–206.
- Marticorena, B., and G. Bergametti (1995), Modeling the atmospheric dust cycle: 1. Design of a soil-derived dust emission scheme, *J. Geophys. Res.*, *100*, 16,415–16,430.
- McPeters, R. D., P. K. Bhartia, A. J. Krueger, J. R. Herman, C. G. Wellemeyer, C. J. Seftor, W. Byerly, and E. A. Celarier (2000), Total Ozone Mapping Spectrometer (TOMS) level-3 data products user's guide, *NASA/TP-2000-209896*, NASA Goddard Space Flight Center, Greenbelt, Md.
- Mlawer, E. J., S. J. Taubman, P. D. Brown, M. J. Iacono, and S. A. Clough (1997), Radiative transfer for inhomogeneous atmospheres: RRTM, a validated correlated-k model for the longwave, *J. Geophys. Res.*, *102*, 16,663–16,682.
- Nickovic, S., and S. Dobricic (1996), A model for long-range transport of desert dust, *Mon. Weather Rev.*, *124*, 2537–2544.
- Nickovic, S., G. Kallos, A. Papadopoulos, and O. Kakaliagou (2001), A model for prediction of desert dust cycle in the atmosphere, *J. Geophys. Res.*, *106*, 18,113–18,130.
- Perez, C., S. Nickovic, J. M. Baldasano, M. Sicard, F. Rocadenbosch, and V. E. Cachorro (2006), A long Saharan dust event over the western Mediterranean: Lidar, Sun photometer observations, and regional dust modeling, *J. Geophys. Res.*, *111*, D15241, doi:10.1029/2005JD006579.
- Prospero, J. M., and T. N. Carlson (1972), Vertical and areal distribution of Saharan dust over the western equatorial North Atlantic Ocean, *J. Geophys. Res.*, *77*, 5255–5265.
- Prospero, J. M., P. Ginoux, O. Torres, S. E. Nicholson, and T. E. Gill (2002), Environmental characterization of global sources of atmospheric soil dust identified with the NIMBUS 7 Total Ozone Mapping Spectrometer (TOMS) absorbing aerosol product, *Rev. Geophys.*, *40*(1), 1002, doi:10.1029/2000RG000095.
- Reiff, J., G. S. Forbes, F. T. M. Spieksma, and J. J. Reijnders (1986), African dust reaching northwestern Europe: A case study to verify trajectory calculations, *J. Appl. Meteorol.*, *25*, 1543–1567.
- Rodriguez, S., X. Querol, A. Alastuey, G. Kallos, and O. Kakaliagou (2001), Saharan dust contributions to PM10 and TSP levels in southern and eastern Spain, *Atmos. Environ.*, *35*, 2433–2447.

- Seaman, N. L. (2000), Meteorological modeling for air-quality assessments, *Atmos. Environ.*, *34*, 2231–2259.
- Seigneur, C., B. Pun, K. Lohman, and S.-Y. Wu (2003), Regional modeling of the atmospheric fate and transport of benzene and diesel particles, *Environ. Sci. Technol.*, *37*, 5236–5246.
- Soil Survey Division Staff (1993), Soil survey manual, in *Soil Conservation Service, U.S. Department of Agriculture Handbook 18*.
- Tegen, I., and I. Fung (1994), Modeling of mineral dust in the atmosphere: Sources, transport, and optical thickness, *J. Geophys. Res.*, *99*, 22,897–22,914.
- Wang, K. Y. (2007), Long-range transport of the April 2001 dust clouds over the subtropical East Asia and the North Pacific and its impacts on ground-level air pollution: A Lagrangian simulation, *J. Geophys. Res.*, *112*, D09203, doi:10.1029/2006JD007789.
- Washington, R. W., M. C. Todd, N. Middleton, and A. S. Goudie (2003), Dust-storm source areas determined by the total ozone monitoring spectrometer and surface observations, *Ann. Assoc. Am. Geogr.*, *93*, 297–313.
- Washington, R., et al. (2006), Links between topography, wind, deflation, lakes and dust: The case of the Bodélé Depression, Chad, *Geophys. Res. Lett.*, *33*, L09401, doi:10.1029/2006GL025827.
- Westphal, D. L., O. B. Toon, and T. N. Carlson (1988), A case study of mobilization and transport of Saharan dust, *J. Atmos. Sci.*, *45*, 2145–2175.
- Wong, S., and A. E. Dessler (2005), Suppression of deep convection over the tropical North Atlantic by the Saharan air layer, *Geophys. Res. Lett.*, *32*, L09808, doi:10.1029/2004GL022295.
- Wu, L. G., S. A. Braun, J. J. Qu, and X. J. Hao (2006), Simulating the formation of Hurricane Isabel (2003) with AIRS data, *Geophys. Res. Lett.*, *33*, L04804, doi:10.1029/2005GL024665.

---

S.-H. Chen, Department of Land, Air, and Water Resources, University of California, One Shields Avenue, Davis, CA 95616, USA. (shachen@ucdavis.edu)

J. Dudhia, Mesoscale and Microscale Meteorology Division/NCAR, 3450 Mitchell Lane, Boulder, CO 80301, USA.

J. S. Kain, National Severe Storms Laboratory, National Weather Center, 120 David L. Boren Blvd., Norman, OK 73072, USA.

T. Kindap, Eurasia Institute of Earth Sciences, Istanbul Technical University, Maslak, 34469 Istanbul, Turkey.

E. Tan, Department of Civil and Environmental Engineering, University of California, Davis, CA 95616, USA.